Retrieving the global distribution of threshold of wind erosion from satellite data and implementing it into the GFDL AM4.0/LM4.0 model

Bing Pu[1, 2, *], Paul Ginoux[2], Huan Guo[2, 3], N. Christine Hsu[4], John Kimball[5], Beatrice Marticorena[6], Sergey Malyshev[2], Vaishali Naik[2], Norman T. O'Neill[7], Carlos Pérez García-Pando[8], Joseph M. Prospero[9], Elena Shevliakova[2], Ming Zhao[2]

[1]Atmospheric and Oceanic Sciences Program, Princeton University, Princeton, New Jersey 08544

[2] NOAA Geophysical Fluid Dynamics Laboratory, Princeton, New Jersey 08540

[3] Cooperative Programs for the Advancement of Earth System Science, University Corporation for Atmospheric Research, Boulder, Colorado, 80301

[4] NASA Goddard Space Flight Center, Greenbelt, Maryland, 20771

[5] Department of Ecosystem and Conservation Sciences, University of Montana, Missoula, Montana 59812

[6]LISA, Universités Paris Est-Paris Diderot-Paris

[7] Département de géomatique appliquée , Université de Sherbrooke

[8] Barcelona Supercomputing Center, Barcelona, Spain, 08034

[9] Rosenstiel School of Marine and Atmospheric Sciences, University of Miami, Miami, Florida, 33149

[*] Current affiliation: Department of Geographical and Atmospheric Science, the University of Kansas, Lawrence, Kansas, 66045

Abstract. Dust emission is initiated when surface wind velocities exceed the threshold of wind erosion. Many dust models used constant threshold values globally. Here we use satellite products to characterize the frequency of dust events and land surface properties. By matching this frequency derived from Moderate Resolution Imaging Spectroradiometer (MODIS) Deep Blue aerosol products with surface winds, we are able to retrieve a climatological monthly global distribution of wind erosion threshold ($V_{threshold}$) over dry and sparsely-vegetated surface. This monthly two-dimensional threshold velocity is then implemented into the Geophysical Fluid Dynamics Laboratory coupled land-atmosphere model (AM4.0/LM4.0). It is found that the climatology of dust optical depth (DOD) and total aerosol optical depth, surface PM_{10} dust concentrations, and seasonal cycle of DOD are better captured over the "dust belt" (i.e. North Africa and the Middle East) by simulations with the new wind erosion threshold than those using the default globally constant threshold. The most significant improvement is the frequency distribution of dust events, which is generally ignored in model evaluation. By using monthly rather than annual mean $V_{threshold}$, all comparisons with observations are further improved. The monthly global threshold of wind erosion can be retrieved under different spatial resolutions to match the resolution of dust models and thus can help improve the simulations of dust climatology and seasonal cycle as well as dust forecasting.

1. Introduction

Mineral dust is one of the most abundant aerosols by mass and plays an important role in the climate system. Dust particles absorb and scatter solar and terrestrial radiation, thus modifying local energy budget and consequently atmospheric circulation patterns. Studies have shown that the radiative effect of dust can affect a wide range of environmental processes. Dust is shown to modulate West African (e.g., Miller and Tegen, 1998; Miller et al., 2004; Mahowald et al., 2010; Strong et al., 2015) and Indian (e.g., Jin et al., 2014; Vinoj et al., 2014; Jin et al., 2015; Jin et al., 2016; Solmon et al., 2015; Kim et al., 2016; Sharma and Miller, 2017) monsoonal precipitation. During severe droughts in North America, there is a positive feedback between dust and the hydrological cycle (Cook et al., 2008, 2009; 2013). African dust is also found to affect Atlantic tropical cyclone activities (e.g., Dunion and Velden, 2004; Wong and Dessler, 2005; Evan et al., 2006; Strong et al., 2018). When deposited on snow and ice, dust reduces the surface reflectivity, enhancing net radiation and accelerating snow and ice melting, and consequently affecting runoff (e.g., Painter et al., 2010; 2018; Dumont et al., 2014). Dust can serve as ice nuclei and affect the formation, lifetime, and characteristic of clouds (e.g., Levin et al., 1996; Rosenfield et al., 1997; Wurzler et al., 2000; Nakajima et al., 2001; Bangert et al., 2012), perturbing the hydrological cycle. Iron and phosphorus enriched dust is also an important nutrient for the marine and terrestrial ecosystems and thus interacts with the ocean and land biogeochemical cycles (e.g., Fung et al., 2000; Jickells et al., 2005; Shao et al., 2011; Bristow et al., 2010; Yu et al., 2015).

Given the importance of mineral dust, many climate models incorporate dust emission schemes to simulate the life cycle of dust aerosols (e.g., Donner et al., 2011;

47 Collins et al., 2011; Watanabe et al., 2011; Bentsen et al., 2013). Mineral dust particles
48 are lifted from dry and bare soils into the atmosphere by saltation and sandblasting. This
49 process is initiated when surface winds reach a threshold velocity of wind erosion. The
50 value of this wind erosion threshold depends on soil and surface characteristics, including
51 soil moisture, soil texture and particle size, and presence of pebbles, rocks, and
52 vegetation residue (e.g., Gillette et al., 1980; Gillette and Passi, 1988; Raupach et al.,
53 1993; Fécan et al., 1999; Zender et al., 2003; Mahowald et al., 2005), and thus varies
54 spatially and temporally (Helgren and Prospero, 1987). Due to a lack of in-situ data at
55 global scale and uncertainties on these dependencies, most dust and climate models
56 prescribe a spatially and temporally constant threshold of wind erosion for surface 10 m
57 wind (e.g., around 6 to 6.5 m s^{-1}) over dry surface for simplicity (e.g., Tegen and Fung,
58 1994; Takemura et al., 2000; Uno et al., 2001; Donner et al., 2011). For instance, in the
59 Geophysical Fluid Dynamics Laboratory coupled land-atmosphere model AM4.0/LM4.0
60 (Zhao et al., 2018a, b), a constant threshold of 6 m s^{-1} is used. On the other hand, some
61 models, such as the ECHAM-HAM, HadGEM2-ES, and ICON-ART, parameterize the
62 constant dry threshold friction velocity (usually a function of soil particle size, soil and
63 air density) or threshold wind velocity with dependencies on soil moisture, surface
64 roughness length, and vegetation coverage (e.g., Takemura et al. 2000; Ginoux et al.
65 2001; Zender et al. 2003; Cheng et al., 2008; Jones et al., 2011; Rieger et al., 2017).
66 The threshold of wind erosion may be approximately inferred using observations.
67 For instance, Chomette et al. (1999) used the Infrared Difference Dust Index (IDDI) and
68 10 m winds reanalysis from the European Centre for Medium-Range Weather Forecasts
69 (ECMWF) between 1990 and 1992 to calculate the threshold of wind erosion over seven

70 sites over the Sahel and Sahara. The IDDI was used to determine whether there was a
71 dust event for subsequently calculating an emission index defined as the number of dust
72 events to the total number of potential events. The distribution of surface wind speed was
73 matched with the emission index, and the threshold of wind erosion was determined
74 when the emission index was around 0.9. The resulting average threshold of wind erosion
75 ranged from 6.63 m s^{-1} at a Sahelian site to about 9.08 m s^{-1} at a Niger site, consistent
76 with the model results by Marticorena et al. (1997).

77 Later, Kurosaki and Mikami (2007) used World Meteorological Organization
78 (WMO) station data from March 1998 to June 2005 to examine the threshold wind speed
79 in East Asia. Using the distribution of surface wind speed and associated weather
80 conditions (i.e., with or without dust emission events), they approximated a dust emission
81 frequency by dividing number of dust events to the total number of observations for each
82 wind bin, and then determined threshold wind speeds at the 5% and 50% levels,
83 corresponding to the most favorable and normal land surface conditions for dust
84 emission, respectively. They found that the derived threshold wind speed varied in space
85 and time, with a larger seasonal cycle in grassland regions, such as northern Mongolia,
86 and smaller seasonal variations in desert regions, such as the Taklimakan and Gobi
87 Deserts and the Loess Plateau. Cowie et al. (2014) applied a similar method over
88 northern Africa, using wind data observed between 1984 and 2012, and focused on
89 threshold winds at the 25%, 50%, and 75% levels.

90 Draxler et al. (2010) derived the distribution of threshold of wind erosion over the
91 U.S. by matching the frequency of occurrence (FoO) of Moderate Resolution Imaging
92 Spectroradiometer (MODIS) Deep Blue (Hsu et al., 2004) aerosol optical depth (AOD)

93 above 0.75 with the FoO of friction velocities extracted from the North American
94 Mesoscale (NAM) forecast model at each grid point. This new threshold and a soil
95 characteristics factor was then incorporated into the Hybrid Single-Particle Lagrangian
96 Integrated Trajectory (HYSPLIT) model (Draxier and Hess, 1998) to forecast dust
97 surface concentrations. It was found that major observed dust plume events in June and
98 July 2007 were successfully captured by the model. Later, Ginoux and Deroubaix (2017)
99 used FoO derived from the MODIS Deep Blue dust optical depth (DOD) record to
100 retrieve the wind erosion threshold of surface 10 m winds over East Asia.

101 For individual dust events, the threshold of friction velocity can also be
102 determined by fitting a second-order Taylor series to dust saltation flux measurements
103 (Barchyn and Hugenholtz, 2011; Kok et al., 2014b).

104 Nonetheless, a global distribution of threshold of wind erosion with observational
105 constraints that may be implemented in climate models is still lacking. In this study, we
106 propose a method to retrieve monthly global threshold of wind erosion (hereafter,
107 $V_{threshold}$) for dry and sparsely-vegetated surface (i.e., under favorable conditions for dust
108 emission) using high-resolution satellite products and reanalysis datasets. This two-
109 dimensional threshold of surface 10 m winds is then implemented into the Geophysical
110 Fluid Dynamics Laboratory (GFDL) coupled land-atmosphere model, AM4.0/LM4.0
111 (Zhao et al., 2018a, b). The benefits of using this spatial and temporal varying threshold
112 in simulating present-day climatology and seasonal cycles of dust are analyzed by
113 comparing the model results with observations.

114 The data and method used to retrieve the threshold of wind erosion are detailed in
115 section 2. The distribution of the derived $V_{threshold}$ and its implication in the climate model

116 is presented in section 3. Section 4 discusses the uncertainties associated with this
117 method, and major conclusions are summarized in section 5.
118
119 **2. Data and Methodology**
120 In this section we first introduce the satellite products, observational data, and
121 reanalyses used to retrieve the threshold of wind erosion and validate model output
122 (section 2.1). The processes to retrieve the threshold of wind erosion are detailed in
123 section 2.2. The uncertainties of $V_{threshold}$ associated with the retrieval criteria and
124 selection of surface wind datasets are discussed in section 2.3. Section 2.4 introduces
125 GFDL AM4.0/LM4.0 model, its dust emission scheme, and simulation designs.
126
127 **2.1 Data**
128 **2.1.1 Satellite products**
129 1) MODIS Aqua and Terra dust optical depth
130 DOD is column-integrated extinction by mineral particles. Here daily DOD is
131 retrieved from MODIS Deep Blue aerosol products (collection 6, level 2; Hsu et al.,
132 2013; Sayer et al., 2013): aerosol optical depth (AOD), single-scattering albedo (ω), and
133 the Ångström exponent (α). All the daily variables are first interpolated to a 0.1° by 0.1°
134 grid using the algorithm described by Ginoux et al. (2010). We require that the single-
135 scattering albedo at 470 nm to be less than 0.99 for dust due to its absorption of solar
136 radiation. This separates dust from scattering aerosols, such as sea salt. Then a continuous
137 function relating the Ångström exponent, which is highly sensitive to particle size (Eck et

al., 1999), to fine-mode AOD established by Anderson et al. (2005; their Eq. 5) is used to separate dust from fine particles. In short, DOD is retrieved using the following equation:

$$DOD = AOD \times (0.98 - 0.5089\alpha + 0.0512\alpha^2) \quad . \quad (1)$$

Details about the retrieval process and estimated errors are summarized by Pu and Ginoux (2018b). High-resolution MODIS DOD products (0.1° by 0.1°) have been used to identify and characterize dust sources (Ginoux et al., 2012; Baddock et al., 2016) and examine the variations in dustiness in different regions (e.g., Pu and Ginoux, 2016, 2017, 2018b).

Following the recommendation from Baddock et al. (2016), who found the dust sources are better detected using DOD with a low-quality flag (i.e., quality assurance flag, QA, equals 1, following the category of retrieval quality flags in MODIS Deep Blue products; Hsu et al., 2013) than that with a high-quality flag (i.e., QA=3) as retrieved aerosol products were poorly flagged over dust source regions, we also use DOD with the flag of QA=1. Both daily DOD retrieved from Aqua and Terra platforms are used by averaging the two when both products are available or using either one when only one product is available. Since Terra passes the equator from north to south around 10:30 am local time (LT) and Aqua passes the Equator from south to north around 13:30 pm LT, an average of the two combines the information from both morning and afternoon hours. This process also largely reduces missing data (Pu and Ginoux, 2018b). This combined daily DOD, hereafter MODIS DOD, is available from January 2003 to December 2015 at a resolution of 0.1° by 0.1° grid. Note that due to the temporal coverage of MODIS products, the diurnal variations in dust (e.g., O'rgill and Sehmel, 1976; Mbourou et al., 1997; Knippertz, 2008; Schepanski et al., 2009) are not included in current study.

2) Soil moisture

Soil moisture is an important factor that affects dust emission (Fécan et al., 1999). Daily surface volumetric soil moisture (VSM) retrievals derived from similar calibrated microwave (10.7 GHz) brightness temperature observations from the Advanced Microwave Scanning Radiometer-Earth Observing System (AMSR-E) onboard the NASA Aqua satellite (from June 2002 to October 2011) and the Advanced Microwave Scanning Radiometer 2 (AMSR2) sensor onboard the JAXA GCOM-W1 satellite (from July 2012 to June 2017) from the University of Montana (Du et al., 2017a; Du et al., 2017b) was used to retrieve wind erosion threshold. Both AMSR-E and AMSR2 sensors provide global measurements of polarized microwave emissions at six channels, with ascending and descending orbits crossing the equator at around 1:30 pm and 1:30 am LT, respectively. The VSM retrievals are derived from an iterative retrieval algorithm that exploits the variable sensitivity of different microwave frequencies and polarizations, and minimizes the potential influence of atmosphere, vegetation, and surface water cover on the soil signal. The VSM record represents surface (top ~2 cm) soil conditions and shows favorable global accuracy and consistent performance (Du et al. 2017b), particularly over areas with low to moderate vegetation cover that are also more susceptible to wind erosion, although cautions are needed when examining long-term trends due to the small biases between AMSR-E and AMSR2. The horizontal resolution of the product is about 25 km by 25 km, and the daily product from January 2003 to December 2015 is used. The ascending and descending obit VSM retrievals are averaged to get the mean VSM for each day.

3) Snow cover

Snow cover may affect dust emission in the mid-latitudes during spring, for instance, over northern China (Ginoux and Deroubaix, 2017). The interannual variation of snow cover is also found to affect dust emission in regions, such as Mongolia (Kurosaki and Mikami, 2004). Here monthly snow cover data from MODIS/Terra level 3 data (Hall and Riggs, 2015) with a resolution of 0.05° by 0.05° from 2003 to 2015 is used. The high spatial resolution of the product is very suitable for this study.

4) Leaf area index (LAI)

Vegetation protects soil from the effects of wind and thus modulates dust emission (e.g., Marticorena and Bergametti, 1995; Zender et al., 2003). While dense vegetation coverage can increase surface roughness and reduce near surface wind speed, the roots of vegetation can increase soil cohesion and further reduce wind erosion. LAI describes the coverage of vegetation with a unit of m^2/m^2, i.e., leaf area per ground area. Here monthly LAI retrieved by Boston University from MODIS onboard Aqua (Yan et al., 2016a; Yan et al., 2016b; via personal communication with Ranga Myneni and Taejin Park; Boston University, 2016) with a resolution of 0.1° by 0.1° from 2003 to 2015 is used. The root mean square error of the product is 0.66, with some overestimation of LAI in sparsely vegetated regions (Yan et al. 2016b; Garrigues et al., 2008).

2.1.2 Reanalysis

Surface wind speed is a critical factor that affects wind erosion. Here 6 hourly 10 m wind speed from the NCEP/NCAR reanalysis (Kalnay et al., 1996, hereafter NCEP1)

on a T62 Gaussian grid (i.e., 192 longitude grids equally spaced and 94 latitude grids unequally spaced) is used. The NCEP1 is a global reanalysis with relatively long temporal coverage, from 1948 to the present. We chose to use the NCEP1 reanalysis mainly because surface winds in the GFDL AM4.0 model are nudged toward the NCEP1, and we preferred to use the reanalysis surface wind that is closest to the model climatology.

ERA-Interim (Dee et al., 2011) is a global reanalysis produced from ECMWF. It provides high spatial resolution (about 0.75° or 80 km) 6-hourly, daily, and monthly reanalysis from 1979 to present day. Soil temperature from the ERA-Interim is used to determine the regions where wind erosion may be prohibited by the frozen surface. Monthly temperature of the first soil layer (0 to 0.07 m) from 2003 to 2015 is used.

In order to quantify the uncertainties of the retrieved threshold wind erosion in association with the selection of reanalysis products, surface 10 m winds from 6-hourly ERA-Interim and hourly ERA5 (Hersbach and Dee, 2016) are both examined. The ERA5 is the latest reanalysis product from the ECMWF, with a horizontal resolution of about 31 km and hourly temporal resolution.

2.1.3 Station data

Multiple ground-based datasets are used to validate AM4.0/LM4.0 simulated aerosol and dust optical depth and surface dust concentrations.

1) AERONET

The AErosol RObotic NETwork (AERONET; Holben et al., 1998) provides quality assured cloud-screened (level 2) aerosol measurements from sunphotometer records. In this paper we used the data products of the version 3.0 AERONET processing routine. To examine model simulated DOD, we used coarse mode AOD (COD; i.e., radius > 0.6 μm) at 500 nm processed by the Spectral Deconvolution Algorithm (O'Neill et al., 2003; hereafter SDA). SDA COD monthly data is first screened to remove those months with less than five days of records. To get the annual means, years with less than five months of records were removed. Only stations with records of at least three years during the period were used to calculate the 2003-2015 climatology (the same time period when MODIS DOD is available). Overall, records from 313 stations were obtained.

AERONET monthly aerosol optical thickness (AOT) data around 550 nm (e.g., 500 nm, 551 nm, 531 nm, 440 nm, 675 nm, 490 nm, 870 nm, etc.) and the Ångström exponents across the dual wavelength of 440-675 nm, 440-870 nm, and 500-870 nm are used to calculate AOD at 550 nm (τ_{550}). If AOT for 551 nm, 555 nm, 531 nm or 532 nm exist, then these values are directly used as AOD 550 nm. Otherwise, the AOT at wavelength λ_A (less than 550 nm), i.e., τ_A , AOT at wavelength λ_B (larger than 550 nm), i.e., τ_B, and Ångström exponent between wavelengths λ_A and λ_B (α) are used to derive AOD 550 nm using the following equations:

$$\tau_{550} = \tau_A \left(\frac{550}{\lambda_A}\right)^{-\alpha} \quad \text{if } \tau_A \text{ is available ,} \tag{2}$$

$$\tau_{550} = \tau_B \left(\frac{550}{\lambda_B}\right)^{-\alpha} \quad \text{if } \tau_B \text{ is available.} \tag{3}$$

252 In a manner similar to the process of screening SDA COD data, monthly AOD
253 550 nm data with less than three days of records in a given month are removed. When
254 calculating the annual means we excluded years having less than five months of records.
255 Finally, to calculate the climatology of 2003-2015, only stations with at least three years
256 of records during this period are used totaling to 351.

257 We also developed a method to derive DOD at 550 nm from AOD at 550 nm
258 based on the relationship between Ångström exponent and fine-mode AOD established
259 by Anderson et al. (2005; their Eq. 5). This adds a few more sites over the Sahel than the
260 SDA COD stations. DOD is calculated by subtracting the fine-mode AOD from the total
261 AOD. Due to the large uncertainties of single scattering albedo in AERONET records
262 over regions where AOD is lower than 0.4 (e.g., Dubovik and King, 2000; Holben et al.,
263 2006; Andrews et al., 2017), we did not use single scattering albedo to screen AOD to
264 further separate dust from scattering aerosols. Therefore, the derived AERONET DOD
265 over coastal stations may be contaminated by sea salt.

266

267 2) RSMAS surface dust concentration

268 The Rosenstiel School of Marine and Atmospheric Science (hereafter RSMAS
269 dataset) at University of Miami collected mass concentration of dust, sea salt, and sulfate
270 over stations globally, with most of stations on islands (Savoie and Prospero, 1989). The
271 dataset has been widely used for model evaluation (e.g., Ginoux et al., 2001; Huneeus et
272 al., 2011).

273 Only stations with records longer than four years were used and of those stations
274 only those years with at least eight months of data are used for calculating climatological

annual means. So, totally 16 stations are used. Station names, locations, and record length are listed in Table S1 of the Supplement. We compare the climatology of annual mean surface dust concentration with model output during 2000-2015. Note that since most station records end earlier than 1998, the dataset largely represents the climatology during the 1980s and 1990s. Thus the discrepancies between model output and the RSMAS data include both model biases and the difference in surface dust concentration from the 1980s to the 2000s.

3) IMPROVE surface fine dust concentration

The Interagency Monitoring of Protected Visual Environments (IMPROVE) network has collected near-surface particulate matter 2.5 ($PM_{2.5}$) samples in the U.S. since 1988 (Malm et al., 1994; Hand et al., 2011). IMPROVE stations are located in national parks and wilderness areas, and $PM_{2.5}$ sampling is performed twice weekly (Wednesday and Saturday; Malm et al., 1994) prior to 2000 and every third day afterwards. Fine dust (with aerodynamic diameter less than 2.5 μm) concentration is calculated using the concentrations of aluminum (Al), silicon (Si), calcium (Ca), iron (Fe), and titanium (Ti) by assuming oxide norms associated with predominant soil species (Malm et al., 1994; their Eq. 5). This dataset has been widely used to study variations in surface fine dust in the U.S. (e.g., Hand et al., 2016; Hand et al., 2017, Tong et al., 2017; Pu and Ginoux, 2018a). Here only monthly data with at least 50% of daily data available in a month (i.e., at least 5 records) are used. Since station coverage over the central U.S. increases after 2002 (e.g., Pu and Ginoux, 2018a), monthly station data from 2002 to 2015 are used and interpolated to a 0.5° by 0.5° grid using inverse distance

298 weighting interpolation. The gridded data are used to evaluate modeled surface fine dust
299 concentrations.
300
301 4) LISA PM_{10} surface concentration
302 Surface PM_{10} concentration from stations from the Sahelian Dust Transect, which
303 was deployed in 2006 under the framework of African Monsoon Multidisciplinary
304 Analysis International Program (Marticorena et al., 2010), were used to examine the
305 surface dust concentration over the Sahelian region. The data are maintained by
306 Laboratoire Interuniversitaire des Systèmes Atmosphériques (LISA) in the framework of
307 the International Network to study Deposition and Atmospheric composition in Africa
308 (INDAAF; Service National d'Observation de l'Institut National des Sciences de
309 l'Univers, France). Three stations are located within the pathway of Saharan and Sahelian
310 dust plumes moving towards the Atlantic Ocean. Here hourly PM_{10} concentrations from
311 these stations, Banizoumbou (Niger, 13.54° N, 2.66° E), Cinzana (Mali, 13.28° N, 5.93°
312 W), and M'Bour (Senegal, 14.39° N, 16.96° W), from 2006 to 2014 are used. The hourly
313 station data are averaged to obtain daily and monthly mean records to compare with
314 model output.
315
316 **2.1.4 Other data**
317 Soil depth from the Food and Agriculture Organization of the United Nations
318 (FAO/IIASA/ISRIC/ISS-CAS/JRC, 2009) on a 0.08° by 0.08° resolution is used to
319 examine whether the soil depth is too shallow (i.e. less than 15 cm) for wind erosion.
320

2.2 Retrieving threshold of wind erosion

The monthly climatological threshold of wind erosion is retrieved by matching the frequency distribution of the MODIS DOD at certain level, namely, DOD_{thresh}, with the frequency distribution of surface 10 m winds from the NCEP1 reanalysis over the period from 2003 to 2015. The process can be summarized by the following steps:

Step1: Since dust is emitted from the dry and sparsely-vegetated surface, the daily DOD data is first masked out to remove the influences of non-erodible factors and unfavorable environmental conditions that are known to prevent dust emission using criteria as follows: daily VSM less than 0.1 cm^3 cm^{-3}; monthly LAI less than 0.3; monthly snow cover less than 0.2% (since snow cover percentage is round-up to integer in MODIS product, this criterion actually requires no snow cover); monthly top-layer soil temperature higher than 273.15 K, i.e., over unfrozen surface; and soil depth thicker than 15 cm. These criteria approximate the most favorable land surface conditions for wind erosion.

Similar criteria have been used in previous studies to detect or confine dust source regions. For instance, Kim et al. (2013) used NDVI less than 0.15, soil depth greater than 10 cm, surface temperature greater than 260 K, and without snow cover to mask topography based dust source function. LAI less than 0.3 has been used as a threshold for dust emission in the Community Land Model (Mahowald et al., 2010; Kok et al., 2014a), while gravimetric soil moisture ranging from 1.01 to 11.2 % depending on soil clay content is recommended to constrain dust emission (Fécan et al., 1999). The uncertainties associated with small variations in the retrieval criteria are further quantified and discussed in section 2.3.

Step 2: Masked daily DOD from Step 1 is then interpolated to a 0.5° by 0.5° grid using bilinear interpolation. This is close to the horizontal resolution of the GFDL AM4.0/LM4.0 model used in this study. Then the cumulative frequency distribution of daily DOD from 2003 to 2015 is derived at each grid point for each month.

Step 3: Daily maximum surface wind speed is first derived from 6-hourly NCEP1 surface winds and then interpolated to a 0.5° by 0.5° grid. Following Ginoux and Deroubaix (2017), we use maximum daily wind speed instead of daily mean wind speed, largely because dust emission only occur when wind speed is strong enough, and the emission magnitude is roughly proportional to the third power of surface wind speed in empirical estimations. The cumulative frequency distribution of daily maximum surface wind from 2003 to 2015 is then calculated at each grid point for each month.

Step 4: A minimum value of DOD (i.e., DOD_{thresh}) is used to separate dust events from background dust. The cumulative frequency (in %) of dust events passing this threshold is compared to the cumulative frequency of surface winds. The minimum surface winds with the same frequency correspond to the threshold of wind erosion, $V_{threshold}$ (see a schematic diagram in Figure S1 in the Supplement). This operation is performed for all grid points for each month. Ginoux et al. (2012) used $DOD_{thresh} = 0.2$ to separate dust events from background dust and quantify the FoO of local dust events. Similarly, $DOD_{thresh} = 0.2$ is used here in major dusty regions (North Africa, Middle East, India, northern China), while for less dusty regions, such as the U.S., South America, South Africa, and Australia, $DOD_{thresh} = 0.02$ is used. The reason to use a lower DOD_{thresh} for less dusty regions is because: i) the overall dust emission in these regions are at least ten times smaller than major dusty regions, such as North Africa (e.g., Huneeus et al.,

2011); ii) the frequency distribution of DOD in these regions also peaks at a much lower DOD band (see discussion in section 3.3). We also tested the DOD_{thresh} = 0.5 for dusty regions and DOD_{thresh} = 0.05 for less dusty regions, and results are discussed in sections 2.3 and 3.1.

Figures 1a-e show the seasonal and annual mean FoO (days when DOD is greater than DOD_{thresh}) using DOD_{thresh}= 0.2 or 0.02. The shaded area covers major dust sources, and the pattern is very similar to that obtained by Ginoux et al. (2012; their Fig. 5), although there are some differences, largely due to the masked DOD (i.e., from Step 1) used in this study and a lower threshold in less dusty regions. The higher FoO in North Africa during summer in comparison with other seasons is consistent with the summer peak of the frequency of dust source activation derived from the Meteosat Second Generation (MSG) images (Schepanski et al., 2007; their Fig. 1). The relatively high value of FoO over the northern Sahel to southern Sahara is also consistent with dust emission frequency derived from the Meteosat Second Generation Spinning Enhanced Visible and InfraRed Imager (Evan et al., 2015; their Fig. 1).

Note that the selections of masking criteria in Step 1 and DOD_{thresh} in Step 4 are empirical and can add uncertainties to this method. Also, we approximate dust emission using cumulative frequency of DOD, which may overestimate dust emission in regions where the contribution of transported dust is significant and thus underestimate the $V_{threshold}$ in those regions. These uncertainties are further discussed in the following section.

2.3 Sensitivities of $V_{threshold}$ associated with retrieval criteria and the selection of reanalysis surface winds

Table 2 shows variations in derived annual mean $V_{threshold}$ averaged in nine dust source regions (see Table 1 for locations) following slight changes of retrieval criteria: soil moisture, LAI, snow coverage, and DOD_{thresh}. When the soil moisture threshold is changed from 0.1 to 0.15 cm^3 cm^{-3} or without the soil moisture constraint, the variations in $V_{threshold}$ are quite small, ranging from 0.01 to about 0.73 m s^{-1} (Table 2). Similarly, changes of LAI criteria from 0.15 to 0.5 m^2 m^{-2} or snow coverage from 0.2% to 10% slightly change $V_{threshold}$ — within 1 m s^{-1} over most regions. On the other hand, $V_{threshold}$ is quite sensitive to the selection of the DOD_{thresh}. $V_{threshold}$ would increase about 1 to 3 m s^{-1} if using DOD_{thresh}= 0.5 for dusty regions (0.05 for less dusty regions) instead of DOD_{thresh}= 0.2 (or 0.02). For instance, using DOD_{thresh}=0.5 increases the averaged annual mean $V_{threshold}$ over the Sahara from 4.6 m s^{-1} (using DOD_{thresh}=0.2) to about 7.6 m s^{-1}.

As mentioned earlier, dust event frequency can be overestimated in regions with high ratio of transported dust and consequently $V_{threshold}$ would be underestimated. Here we provide a rough estimation about the influence of transported dust on $V_{threshold}$ over North Africa. It is hard to separate local dust emission and transported dust in the column integrated DOD, so we use surface DOD data (sDOD; personal communication with Juliette Paireau), i.e., DOD form surface to about 400 m, to approximate the component of DOD due to local emission. sDOD is derived by using DOD vertical profile from the Cloud-Aerosol Lidar with Orthogonal Polarization (CALIOP; Winker et al., 2004; Winker et al., 2007) to first calculate a ratio of near surface DOD (0~400 m) to total DOD (0~12km) and then multiplying the ratio to daily MODIS Aqua DOD over North

Africa from 2003-2014. Using sDOD, $V_{threshold}$ over the Sahel would increase from 3.2 to 6.0 m s^{-1}, while over the Sahara, $V_{threshold}$ would increase from 4.6 to 7.7 m s^{-1} (Table 2, last column).

How $V_{threshold}$ would change when using surface winds from different reanalyses are examined in Table 3. Surface winds from the ERA-Interim produce higher $V_{threshold}$ than the NCEP1 by 0.2 to 2.2 m s^{-1}. Using surface winds from the ERA5 also would increase $V_{threshold}$ by 1 to 1.6 m s^{-1} over North Africa and about 1.5 m s^{-1} over Australia but create smaller differences in other regions.

In short, $V_{threshold}$ are less sensitive to small changes in the criteria to define a favorable, dry, and sparsely vegetated land surface condition for wind erosion than the choices of DOD_{thresh} or surface wind speeds from different reanalysis products. Over North Africa, not separating transported dust from total DOD may lead to an underestimation of $V_{threshold}$ up to 3 m s^{-1} based on a rough estimation. However, due to the large uncertainties in quantifying transported dust and the regional converge of sDOD dataset, we chose not to incorporate the results from sDOD to the global $V_{threshold.}$

2.4 Simulation design

We will examine if the observation-constrained, spatial and temporal varying $V_{threshold}$ would improve dust simulation in the GFDL AM4.0/LM4.0. The AM4.0/LM4.0 is a coupled land-atmosphere model newly developed at GFDL (Zhao et al., 2018a,b). It uses the recent version of the GFDL Finite-Volume Cubed-Sphere dynamical core (FV^3; Putman and Lin, 2007), which is developed for weather and climate applications with both hydrostatic and non-hydrostatic options. Some substantial updates have been

incorporated into the AM4.0, such as an updated version of the model radiation transfer code, an alternate topographic gravity wave drag formulation, a double-plume model representing shallow and deep convection, a "light" chemistry mechanism, and modulation on aerosol wet removal by convection and frozen precipitation (Zhao et al., 2018a,b). Here we used a model version with 33 vertical levels (with model top at 1hPa) and cube-sphere with 192×192 grid boxes per cube face (approximately 50 km grid size).

The aerosol physics is based in large part on that of the GFDL AM3.0 (Donner et al., 2011), but with a simplified chemistry where ozone climatology from AM3.0 simulation (Naik et al., 2013) is prescribed. AM4.0 simulates the mass distribution of five aerosols: sulfate, black carbon, organic carbon, dust, and sea salt. Dust is partitioned into five size bins based on radius: 0.1~1 μm (bin 1), 1~2 μm (bin 2), 2~3 μm (bin 3), 3~6 μm (bin 4), and 6~10 μm (bin 5). The dust emission scheme follows the parameterization of Ginoux et al. (2001), as shown in the following equation:

$$F_p = C \times S \times s_p \times V_{10m}^2 \, (V_{10m} - V_t) \qquad (\text{if } V_{10m} > V_t), \qquad (4)$$

where F_p is flux of dust of particle size class p, C is a scaling factor with a unit of μg s^2 m^{-5}, here C is set to 0.75×10^{-9}. S is the source function based on topographic depressions (Ginoux et al., 2001), s_p is fraction of each size class, and V_{10m} is surface 10 m wind speed, and $V_t = 6$ m s^{-1} is the threshold of wind erosion.

Three simulations with prescribed sea surface temperature (SST) and sea ice (Table 4) were conducted from 1999 to 2015, with the first year discarded for spin up. The Atmospheric Model Intercomparison Project (AMIP)-style SST and sea ice data (Taylor et al., 2000) are from the Program for Climate Model Diagnosis and

458 Intercomparison (PCMDI), which combined HadISST (Rayner et al., 2003) from UK Met
459 Office before 1981 and NCEP Optimum Interpolation (OI) v2 SST (Reynolds et al.,
460 2002) afterwards. The surface winds in the simulations are nudged toward the NCEP1
461 reanalysis with a relaxation timescale of 6 hours (Moorthi and Suarez, 1992). Note that
462 the nudged surface winds are actually weaker than the surface wind speed simulated by
463 the standard version of AM4.0/LM4.0 without nudging, so the overall magnitude of dust
464 emission is lower than the standard version. Here we choose not to retune the dust
465 emission scheme but instead test the usage of $V_{threshold}$, which theoretically provides a
466 more physics-based way to improve dust simulation. We also choose to keep the tuning
467 factor C (Eq. 4) the same in all simulations to better examine the effects of implementing
468 the newly developed $V_{threshold}$.

469 In the Control run, the default model setting is used for dust emission, with a
470 prescribed 6 m s^{-1} threshold of wind erosion (cf. Ginoux et al., 2019). In the V_{thresh}12mn
471 simulation, the observation based climatological monthly $V_{threshold}$ is used to replace the
472 constant wind erosion threshold. The default source function S in Eq. 4 only allows dust
473 emission over bare ground by masking out regions with vegetation cover. Since LAI
474 masking is already applied in the retrieval of $V_{threshold}$ (i.e., LAI<0.3), we choose to use a
475 source function that is the same as the default source function S but without vegetation
476 masking, i.e., S' (Figure S2 in the supplement). This allows the influence of the spatial
477 and temporal variations in $V_{threshold}$ to be fully examined. The combination of source
478 function S' and $V_{threshold}$ also extends dust source from bare ground to sparsely vegetated
479 area as outlined by $V_{threshold}$, e.g., over central North America, central India, and part of
480 Australia, and can increase dust emission in these regions. The pattern of extended dust

source area largely resembles the vegetated dust source identified by Ginoux et al. (2012; their Fig. 15b) and Kim et al. (2013; their Fig. 9). All the other settings are the same as the Control run. The V_{thresh}Ann simulation is the same as the V_{thresh}12mn but uses the annual mean $V_{threshold}$ for each month. Since the same SST and sea ice are prescribed for all simulations and land use dose not change much during the short duration of simulation, the differences in simulated dynamic vegetation by LM4.0 among the three simulations are actually very small and can be ignored (see Figures S3-4 in the Supplement).

3. Results

3.1 Thresholds of wind erosion with DOD_{thresh} = 0.2 (or 0.02) and DOD_{thresh} = 0.5 (or 0.05)

Figures 1f-j show the derived threshold of wind erosion for each season and annual mean using DOD_{thresh} =0.2 (or 0.02). The seasonal variations in wind erosion threshold are largely due to the variations in DOD and surface wind frequency distributions that are in turn associated with variations in land surface features, such as soil moisture, soil temperature, snow cover, and vegetation coverage in each month. $V_{threshold}$ is generally lower in MAM and JJA (SON and DJF) for Northern (Southern) Hemisphere dusty regions than in other seasons, consistent with higher FoO in these seasons. $V_{threshold}$ values are also lower in regions with a high FoO (Figs. 1a-e).

The distributions of $V_{threshold}$ for annual mean (black bars) and dusty seasons (color lines; MAM and JJA for the Northern Hemisphere and SON and DJF for the Southern Hemisphere) for each dust source region (see Fig. 1f and Table 1 for locations)

504 are shown in Figs. 2a-i. In the Sahel and Sahara, the annual mean $V_{threshold}$ peaks around 4
505 and 4.5-5.5 m s^{-1}, respectively (Figs. 2a-b). This magnitude is lower than indicated from
506 previous studies based on station observations in the region, e.g., Helgren and Prospero
507 (1987) found the threshold velocity over eight stations in Northwest Africa ranged from
508 6.5 to 13 m s^{-1} during summer in 1974. Chomette et al. (1999) and Marsham et al. (2013)
509 also reported higher wind erosion thresholds around 6-9 m s^{-1} at individual stations. On
510 the other hand, Cowie et al. (2014) found that the annual threshold of wind erosion at the
511 25% level, i.e., when surface condition is favorable for dust emission, can be lower than 6
512 m s^{-1} at some sites in the Sahel (their Fig. 5). Several factors may contribute to the
513 discrepancies. Firstly, studies suggest that reanalysis datasets may underestimate surface
514 wind speed in spring and for monsoon days in Africa (e.g., Largeron et al., 2015), and
515 therefore could lead to a lower value of $V_{threshold}$ than that derived from station
516 observations. In fact, Bergametti et al. (2017) found even 3-hourly wind speed record at
517 stations may miss short events with high wind speed. As shown in Table 3, among the
518 reanalysis wind products tested here, the NCEP1 actually produced a lower $V_{threshold}$ in
519 North Africa than the other two reanalyses. Secondly, using DOD frequency to
520 approximate dust emission may lead to an overestimation of dust emission over regions
521 such as the southern Sahel where transported dust is a large component and consequently
522 an underestimation of $V_{threshold,}$ Based on our rough estimation, $V_{threshold}$ in North Africa
523 can be underestimated by up to 3 m s^{-1} (section 2.3). In addition, different analysis time
524 periods or methods to retrieve the wind erosion threshold may also contribute to the
525 differences.

526 The annual mean $V_{threshold}$ in Arabian Peninsula is a bit higher, with mean values
527 at 5.2 m s^{-1} (Fig. 2c). The $V_{threshold}$ over northern China is even higher, with an annual
528 mean of 7.8 m s^{-1}. This is consistent with the results of Kurosaki and Mikami (2007),
529 who found that under favorable land surface conditions the threshold wind speed ranges
530 from 4.4± 0.6 m s^{-1} in Taklimakan Desert to 6.9± 1.2 m s^{-1} over the Loess Plateau and
531 around 9.8± 1.6 m s^{-1} in the Gobi Desert. These values are also consistent with Ginoux
532 and Deroubaix (2017) who found that regional mean wind erosion threshold over
533 northern China ranges from 6.5 to 9.1 m s^{-1}. In India, the $V_{threshold}$ peaks at about 4.5 m s^{-1} and 6.5 m s^{-1}, respectively (Fig. 2e). The second peak is probably related to
535 anthropogenic dust sources over the central Indian subcontinent (Ginoux et al., 2012).
536 We also note that in the Northern Hemisphere, the $V_{threshold}$ in dusty seasons is shifted
537 towards lower values than the annual mean (blue and green lines in Figs. 2a-f), but is
538 similar to the annual mean in the Southern Hemisphere (especially South America and
539 Australia), indicating stronger influences of surface variability in the Northern
540 Hemisphere.

541 Fig. 3 shows the seasonal mean and annual mean global $V_{threshold}$ using DOD_{thresh}
542 =0.5 (or 0.05). The corresponding distribution of annual mean $V_{threshold}$ in each region is
543 shown in Figure S5 in the Supplement. The derived $V_{threshold}$ is generally higher than
544 using DOD_{thresh} =0.2 (or 0.02), especially over North Africa, the Arabian Peninsula,
545 India, and Asia (Fig. 3 and Table 2). The results are thus closer to previous station based
546 studies over North Africa. On the other hand, over northern China, $V_{threshold}$ is around or
547 greater than 8 m s^{-1} (Fig. 3e), slighter higher than previous estimates (e.g., Kurosaki and
548 Mikami 2007; Ginoux and Deroubaix 2017).

549 In the following section, we will exam if the spatial and temporal varying $V_{threshold}$
550 would improve model simulation of DOD spatial pattern, seasonal variations, frequency
551 distribution and surface dust concentrations in the GFDL AM4.0/LM4.0. Results using
552 $V_{threshold}$ with DOD_{thresh} =0.2 (or 0.02) are shown in sections 3.2 to 3.3 and results using
553 $V_{threshold}$ with DOD_{thresh} =0.5 (or 0.05) are briefly discussed in section 4.
554
555 **3.2 $V_{threshold}$ in the GFDL AM4.0/LM4.0 model**
556 In this section we analyze the model output using the default setting (Control;
557 Table 4), 12-month (V_{thresh}12mn), and annual mean $V_{threshold}$ (V_{thresh}Ann) by comparing
558 model results with multiple observational datasets and MODIS DOD..
559
560 **3.2.1 Climatology of AOD and DOD**
561 In order to compare the model results with observations, we first show the
562 climatology of AERONET AOD and COD from 2003 to 2015. The length of records for
563 each station is shown in Figure S6 in the Supplement. As shown in Figure 4, annual mean
564 global AOD is highest over Africa, the Arabian Peninsula, Indian subcontinent, and
565 Southeast Asia. In the latter two regions, high sulfate concentrations (e.g., Ginoux et al.,
566 2006) and organic carbon from biomass burning in Southeast Asia (e.g., Lin et al., 2014)
567 contribute substantially to the total AOD. The SDA COD shows the optical depth due to
568 coarse aerosols, which includes both dust and sea salt, and sea salt over coastal regions or
569 islands can be a major contributor. Here, high values (>0.2) are largely located over
570 dusty regions such as North Africa, the Arabian Peninsula, and northern India (Fig. 4b).

571 Figures 5a-b show the scatter plots of modeled AOD and COD in the Control run
572 versus AERONET AOD and COD, respectively. Here column-integrated extinction from
573 both dust and sea salt is used to calculated COD in the model. The relative differences
574 (%) between AM4.0 output and AERONET station data are also shown (Figs. 5c-d). The
575 percentage of DOD to total COD in the model is displayed at the bottom (Fig. 5e). The
576 simulated AOD is lower than that from the AERONET over North Africa, the Middle
577 East, and western India, largely due to low values of COD simulated in these regions
578 (Fig. 5d). Besides these regions, the COD over North America, South America, South
579 Africa, and northern Eurasia is also, for the most part, underestimated by the model. Dust
580 is the dominant contributor to the COD value over most of these low COD regions,
581 except over the central to eastern North America and central South America (Fig. 5e).
582 COD (and effectively DOD given its dominance in most regions) was better
583 simulated in the subsequent model run using a prescribed 12-month $V_{threshold}$ in terms of
584 both magnitude and spatial pattern. Figure 6 shows the results from the V_{thresh}12mn
585 simulation. COD is better captured while the AOD effectively moves from a negative to a
586 slightly positive bias (Figs. 6a-d). Most sites over North Africa and the Middle East show
587 a relatively small difference with AERONET COD (Fig. 6d). Over the Indian
588 subcontinent, COD is overestimated, while over North America excluding the east coast,
589 northern Eurasia, and part of South America, COD is also better captured than in the
590 Control run.
591 These improvements are largely associated with a better simulation of DOD in the
592 “dust belt” (i.e., North Africa and the Middle East). Figure 7 shows the DOD at 550 nm
593 derived from AERONET AOD (see methodology for details) versus that from the

V_{thresh}12mn simulation. Over most stations in the Sahel, Mediterranean coasts, and central Middle East, the relative differences between modeled and observed DOD is within ± 25%.

Figure 8 shows the regional averaged annual mean DOD over nine dusty regions from MODIS and three simulations. The Control run largely underestimates DOD in all regions, while the magnitude of DOD is better captured in the V_{thresh}12mn and V_{thresh}Ann simulations, although slightly overestimated in the Sahel and greatly overestimated over Australia. In general, DOD simulated by the V_{thresh}Ann run using a constant annual mean $V_{threshold}$ is higher than that simulated by the V_{thresh}12mn run, consistent with the higher dust emission in the V_{thresh}Ann run (Table S2 in the Supplement). Lack of soil moisture constraint in the model, which is a very important element in capturing the variation of DOD in Australia (Evans et al., 2016), may contribute to the large overestimation of DOD in Australia.

3.2.2 Climatology of surface dust concentration

While DOD is a key parameter associated with the climate impact of dust, surface dust concentration is an important factor affecting local air quality. Here we compare the modeled surface dust concentration with RSMAS station observations. Model output is averaged from 2000 to 2015 to form the annual climatology. Consistent with the DOD output, the Control run largely underestimates surface dust concentrations at almost all of the sites (except sites 9 and 15; Figure 9 top panel). The underestimation is reduced in the V_{thresh}Ann simulation (Fig. 9, middle panel), with seven stations having model/observation ratios between 0.5 and 2 (white triangles). Over the coastal U.S. (e.g.,

sites 16 and 13), dust concentrations are overestimated, consistent with the overestimation of DOD over the U.S. and the Sahel (Fig. 8). Dust concentrations in Australia and the east coast of China are also overestimated by more than five-folds. Surface dust concentration is further improved in the V_{thresh}12mn simulation (Fig. 9, bottom), with eight stations showing a model/observation ratio between 0.5 and 2 and only four stations overestimating or underestimating dust concentrations by more than five times.

Simulated surface fine dust concentration (calculated as dust bin 1+0.25×dust bin 2) in the U.S. is compared with gridded IMPROVE data (Figure 10). While the Control run largely underestimates surface fine dust concentration, the simulated concentration is overall too high in the V_{thresh}Ann run. The spatial pattern of fine dust concentration is better captured in the V_{thresh}12mn run, with higher values over the southwestern U.S., but the magnitude is still overestimated, and additional dust hot spots are simulated over the northern Great plains and the Midwest, which are not shown in the IMPROVE data. Such an overall overestimation may be attributed to lack of soil moisture modulation in the dust emission scheme. The way in which dust bins are partitioned in the model can add uncertainties to model's representation of surface fine dust concentrations as well. On the other hand, the relatively low spatial coverage of IMPROVE sites over the northern Great Plains and Midwest (e.g., Pu and Ginoux, 2018a) may also add uncertainties to the data itself.

640 **3.2.3 Seasonal cycles**

641 Figure 11 compares the seasonal cycle of DOD from three simulations with
642 MODIS DOD in nine dusty regions. The seasonal cycle of gridded AERONET COD (as
643 an approximation to DOD; on a 0.5° by 0.5° grid) is also shown. Since the gridded COD
644 may have large uncertainties over regions with only a few stations, such as the Sahel,
645 Sahara, northern China, and South Africa, MODIS DOD is used as the main reference in
646 the comparison. Seasonal cycles are better captured by the V_{thresh}12mn simulation in the
647 Sahel, the Sahara, and the Arabian Peninsula (Figs. 11a-c), although the spring and
648 summer peak in the Sahel is overestimated and winter minimum in the Sahara is
649 underestimated. The MAM peak of MODIS DOD in northern China is missed by both
650 V_{thresh}12mn and V_{thresh}Ann simulations (Fig. 11d), while the JJA peak over India is
651 largely overestimated (Fig. 11e). Over the U.S. dusty region, the seasonal cycle in the
652 V_{thresh}12mn simulation is slightly underestimated compared to MODIS DOD but
653 overestimated from May to August in the V_{thresh}Ann simulation (Fig. 11f). DOD is
654 underestimated in South Africa in all three simulations (Fig. 11g). Over South America,
655 the peak from October to February is roughly captured by the V_{thresh}12mn run but is
656 overestimated by the V_{thresh}Ann run (Fig. 11h). The seasonal cycles of DOD in Australia
657 are very similar in all three simulations and largely resemble that in the MODIS, although
658 both the V_{thresh}12mn and V_{thresh}Ann simulations overestimate the DOD by about an order
659 of magnitude.

660 Figure 12 shows the seasonal cycle of COD from 12 AERONET SDA sites over
661 North Africa and nearby islands (see Figure S7 in the Supplement for site locations)
662 along with MODIS DOD and DOD simulated in three runs. The magnitude of

AERONET COD and MODIS DOD in these sites are very similar, despite missing values at sites 1, 4, 5, 8, 11, and a smaller value at site 2 in MODIS. Over most of the sites, the seasonal cycle is better captured in the V_{thresh}12mn and V_{thresh}Ann simulations than the Control run, although the peak over Cairo_EMA_2 (site 12) is slightly underestimated, which is consistent with the underestimation of annual mean DOD in the area (Fig. 7).

We also examined the seasonal cycle of PM_{10} surface concentration at three Sahelian INDAAF stations (see Figure S7 in the Supplement for site locations) from the LISA project. Figures 13a-c show PM_{10} surface dust concentration (here dust dominates total PM_{10} concentration) from the Control, V_{thresh}12mn, and V_{thresh}Ann simulations versus observed PM_{10} concentration from three LISA sites. PM_{10} concentrations in these sites peak during boreal winter and spring and reach minima from July to September. These seasonal variations are associated with the dry northerly Harmattan wind in boreal winter and spring that transports Saharan dust southward to the Guinean coast and the scavenging effect of monsoonal rainfall in boreal summer that removes surface dust (Marticorena et al., 2010; Fiedler et al., 2015). While the Control run does not capture the seasonal cycles in these sites, the V_{thresh}12mn run largely captures the spring peak and summer minimum, although the magnitude is overestimated. In all three sites, the simulated concentration in the V_{thresh}Ann run is larger than that in the V_{thresh}12mn run, especially in boreal fall to early spring. Such an overestimation is probably due to the prescribed constant annual mean $V_{threshold}$, which is lower than it would be during the less dusty season (i.e., boreal fall to winter) and thus increases dust emission and surface concentration.

685 Figs. 13d-f show the seasonal cycle of DOD from three AERONET sites co-
686 located with LISA INDAAF stations and from three simulations. The V_{thresh}12mn and
687 V_{thresh}Ann simulations largely captured the seasonal cycle of DOD at these sites. The
688 overestimation of near surface PM_{10} dust concentration (Figs. 13a-c) and the generally
689 well-captured column integrated DOD (Figs. 13d-f) indicate that model likely
690 underestimates dust concentration in the atmospheric column above the surface, which
691 needs further investigation in future studies.
692
693 **3.2.4 A dust storm over U.S. northern Great Plains on October 18th, 2012**
694 Can the AM4.0/LM4.0 with prescribed $V_{threshold}$ better represent individual dust
695 events? Here we examine a major dust storm captured by MODIS Aqua true color-image
696 on Oct. 18th, 2012 (https://earthobservatory.nasa.gov/images/79459/dust-storm-in-the-
697 great-plains) over the U.S. northern Great Plains. There was a severe drought in 2012
698 with anomalously low precipitation centered over the central U.S. (e.g., Hoerling et al.,
699 2014). The dry conditions favored dust storm development when there were intensified
700 surface winds. However, this storm was not predicted by the forecast models, such as the
701 Goddard Earth Observing System version 5 (GEOS-5; Rienecker et al., 2008) and Navy
702 Aerosol Analysis Prediction System (NAAPS; Witek et al., 2007; Reid et al., 2009;
703 Westphal et al., 2009).
704 As shown in Figure 14, MODIS DOD also captures this event, with a peak value
705 above 0.5 over southwest Nebraska and northern Kansas on Oct. 18th, 2012. The
706 V_{thresh}12mn run also largely captures this event (Fig. 14 bottom panel), although the
707 Control run totally misses it (not shown). In the model, the dust storm appears in South

Dakota and Nebraska on Oct. 17th, 2012, along with the anomalous southwesterly winds. It reaches a maximum on Oct. 18th, in association with intensified anomalous southwesterly winds at the surface and an anomalous low-pressure system at 850 hPa (Figure S8 in the Supplement). Note that the modeled dust storm center is located a bit northeastward compared to the MODIS DOD pattern and it also has greater magnitude and covers a larger area. On Oct. 19th, both the anomalous low-pressure system and surface wind speeds weaken and the dust storm dissipates, with slightly elevated DOD levels over a region extending over the lower Mississippi River basin and the Midwest. This is somewhat consistent with MODIS records, which also shows slightly higher DOD levels over Tennessee and northern Alabama on Oct. 19th, regardless of large area of missing values.

3.3 Frequency distribution of DOD in the model versus that from MODIS

Figure 15 shows the frequency distribution of regional mean DOD during one dusty season (MAM in the Northern Hemisphere and SON in the Southern Hemisphere) for nine regions. Results from MODIS, the Control, and V_{thresh}12mn runs are shown in black, blue, and orange lines, respectively. In most dusty regions, such as the Sahara, Sahel, Arabian Peninsula, India, and northern China, MODIS DOD frequency largely peaks between 0.2 to 0.4, while DOD frequency peaks at a much lower level between 0.02 to 0.08 in less dusty regions, such as the U.S., South America, South Africa and Australia. This also justifies our selection of DOD_{thresh} of 0.02 (instead of 0.2) in the less dusty regions. The DOD distribution in the Control run is biased low and peaks around 0.05 in those dusty regions and between 0 and 0.01 in less dusty regions. The frequency

731 is much better captured in the V_{thresh}12mn run over the Arabian Peninsula and the Sahel,
732 slightly improved but still biased low over the Sahara, northern China, India, and the U.S.
733 The modeled frequency in the V_{thresh}12mn run is biased high in Australia (peaks outside
734 the maximum of x-axis, not shown) and shows little improvement over South Africa and
735 South America. The overall improvement of DOD frequency using the time-varying 2D
736 $V_{threshold}$ occurs mostly over major dusty regions, which is consistent with the
737 improvements in DOD climatology and seasonal cycle in the model simulations.
738
739 **4. Discussion**
740 A global distribution of the threshold of wind erosion is retrieved using high
741 resolution MODIS DOD and land surface constraints from relatively high–resolution
742 satellite products and reanalyses. While this climatological monthly $V_{threshold}$ provides
743 useful information about the spatial and temporal variations in wind erosion threshold,
744 there are some uncertainties associated with it. Here DOD frequency is derived using
745 MODIS and other satellite products, thus the uncertainties in the satellite products are
746 inherited in the derived DOD frequency distribution. Due to the cloud screening
747 processes of MODIS products, dust activities over cloud-covered regions may be
748 underestimated. Also, DOD frequency is derived based on daily observations over a 13-
749 year record, so that some variability of dust emission associated with alluvial sediments
750 deposited by seasonal flooding may be not captured. Diurnal variability of dust emission
751 and short-duration events such as haboobs are also not included. Since DOD is a column
752 integrated variable, it includes both local emitted and remotely transported dust. When
753 using DOD frequency distribution to approximate dust emission, it may overestimate dust

emission in regions where transported dust is dominated and lead to an underestimation of $V_{threshold}$. Future studies to better quantify the influences of transported dust would further improve quantitative retrieval of $V_{threshold,}$

Previous study found that over regions such as North Africa, reanalysis products may underestimate surface wind speed in spring and monsoon seasons but overestimate it during dry nights (e.g., Largeron et al., 2015). This is largely because mechanisms such as density current that can enhance surface wind speed are not parameterized in the atmospheric models to produce the reanalysis products, while coarse spatial and temporal sampling may also contribute to the underestimation of reanalysis wind speeds. The selection of surface winds from different reanalysis products also affects the derived $V_{threshold.}$ Among the three reanalyses examined here, $V_{threshold,}$ derived from the NCEP1 reanalysis shows slightly lower values than others.

In addition, $V_{threshold}$ is derived by matching the frequency distribution of DOD at certain levels (i.e., DOD_{thresh}) with the frequency distribution of daily maximum wind. An issue is that selecting a value of DOD_{thresh} is quite empirical. The influences of soil properties such as soil cohesion, particle size, and particle compositions on the threshold of wind erosion (e.g., Fécan et al., 1999; Alfaro and Gomes, 2001; Shao, 2001; Kok et al., 2014b) are not explicitly examined here and will need further investigation.

The influences of $V_{threshold}$ on AM4.0/LM4.0 results are twofold. On the one hand, it modifies the default constant threshold of wind erosion (V_t in Eq. 4) by allowing spatial and temporal variations of wind erosion threshold over bare ground, i.e., within the domain of default dust source function S (Figs. S9a-e in the Supplement). On the other hand, it slightly extends the potential emission area to sparsely-vegetated regions as

outlined by $V_{threshold}$ (Figs. S9f-j in the Supplement). Which effect dominates? Taking the V_{thresh}12mn simulation as an example, Figure S10 shows the differences of dust emission with the Control run. The increase of dust emission in the V_{thresh}12mn simulation (also summarized in Table S2 in the Supplement) is largely associated with the enhanced emission over the bare ground (Figs. S10a-e in the Supplement), mainly over the regions with reduced wind erosion threshold (Figs. S9a-e in the Supplement). The increased emission over sparsely-vegetated area over regions such as the southern Sahel, India, and Australia plays a minor role. This is consistent with Kim et al. (2013), who found global dust emission in the Georgia Institute of Technology–Goddard Ozone Chemistry Aerosol Radiation and Transport (GOCART) model is dominated by emission from bare ground.

The major benefit of using the spatial and temporal varying $V_{threshold}$ is that it improves the simulation of DOD spatial pattern (Figs. 6-7), seasonal cycle (Figs. 11-13), and frequency distribution (Fig. 15) as well as the spatial pattern of surface dust concentrations (Figs. 9-10), which cannot be achieved by simply modifying the global tuning factor (i.e., C in Eq. 4) to fit the observations such as surface concentrations or optical depth.

The default setting in the Control run produced a relatively low global dust emission (978 Tg yr^{-1}) in comparison with the AeroCom multi-model median (1123 Tg $yr^{-1;}$ Huneeus et al. 2011) or a previous estimation based on MODIS DOD (1223 Tg yr^{-1}; Ginoux et al. 2012). So we also conducted a test run (Control II) to increase global dust emission in the Control run to about 1232 Tg yr^{-1} by enlarging C in Eq. 4. The magnitude of DOD slightly increases, e.g., over the Sahel annual mean increases from 0.07 to 0.09,

799 however, there's no improvement in terms of seasonal cycle or spatial pattern, as
800 expected.

801 We also examined the performance of $V_{threshold}$ using DOD_{thresh}= 0.5 (or 0.05) in
802 the AM4.0/LM4.0. Similarly, we conducted simulations with 12-month $V_{threshold}$
803 (V_{thresh}12mn II) and annual mean $V_{threshold}$ (V_{thresh}Ann II), all using the same tuning factor
804 as in the Control II. We found similar improvement in DOD seasonal cycle and weaker
805 improvement in DOD spatial pattern and frequency distribution and surface dust
806 concentrations (except with the IMPROVE data over the U.S. and surface concentrations
807 over the Sahel, where dust concentrations are previously overestimated). This is largely
808 because higher $V_{threshold}$ leads to lower global dust emissions in the V_{thresh}Ann II (1961
809 Tg yr^{-1}) and V_{thresh}12mn II simulations (1705 Tg yr^{-1}) and overall lower DOD. Over
810 Mediterranean coast, Europe, and northern Asia, DOD spatial pattern is not as well
811 captured in the V_{thresh}12mn II run as in the V_{thresh}12mn run, likely due to relatively high
812 $V_{threshold}$ in these regions.

813

814 **5. Conclusion**

815 While dust aerosols play important roles in the Earth's climate system, large
816 uncertainties exist in modeling its lifecycle (e.g., Huneeus et al., 2011; Pu and Ginoux,
817 2018b). Constant thresholds of wind erosion are widely used in climate models for
818 simplicity. Here, high-resolution MODIS Deep Blue dust optical depth (DOD) and
819 surface wind speeds from the NCEP1 reanalysis, along with other land surface factors
820 that affect wind erosion, such as soil moisture, vegetation cover, snow cover, soil
821 temperature, and soil depth, were used to develop a time-varying two-dimensional

822 climatological threshold of wind erosion, $V_{threshold}$, based on the seasonal variations of
823 DOD and surface wind distribution frequencies. $V_{threshold}$ is generally lower in dusty
824 seasons, i.e., MAM and JJA (SON and DJF) in the Northern (Southern) Hemisphere.

825 The climatological monthly $V_{threshold}$ was then incorporated into the GFDL
826 AM4.0/LM4.0 model to examine the potential benefits relative to the use of a constant
827 threshold. In comparison with the simulation using the default setting of a globally
828 constant threshold of wind erosion (6 m s^{-1}), both the magnitude of DOD and surface dust
829 concentrations are increased and closer to observations. However, different from
830 modifying the global tuning factor (i.e., C in Eq. 4) to increase the overall magnitudes of
831 DOD or surface dust concentrations, we found the spatial and temporal varying $V_{threshold}$
832 largely improves the simulation of the spatial pattern, seasonal cycle, and frequency
833 distribution of DOD over Northern Hemisphere dusty regions, such as North Africa and
834 the Arabian Peninsula, and slightly improved over India, the western to central U.S., and
835 northern China. The seasonal cycle of DOD are also slightly improved in South America,
836 although change little in South Africa. The incorporation of $V_{threshold}$ leads to an
837 overestimation of DOD in Australia, likely in association with the absence of soil
838 moisture constraints on dust emission in the model.

839 The spatial pattern of surface dust concentrations is also improved when time-
840 varying $V_{threshold}$ is incorporated. The fine dust concentration in the U.S. is also better
841 captured, with the maximum of annual mean largely located over the southwestern U.S.,
842 although the magnitude is overestimated.

843 A constant annual mean $V_{threshold}$ is also tested in the model, and is found to
844 overestimate DOD over dusty seasons in the Arabian Peninsula, U.S., India, Australia,

and South America. Surface PM_{10} concentrations in the Sahel during boreal fall and winter seasons are also largely overestimated with this setting. The results indicate the importance of including the seasonal cycle of $V_{threshold}$ in the model. Using time-varying $V_{threshold}$, the model was also able to capture a strong dust storm in the U.S. Great Plains in October 2012, which created deadly accidents, while some dust forecasting models failed to reproduce it.

Finally, this method to retrieve global threshold of wind erosion can be conducted under different resolutions or surface wind reanalsyses or being applied to surface fiction velocity datasets to match the resolution/scheme of dust models and may help improve their simulations and forecasting of dust distribution. As discussed in section 4, there are uncertainties associated with this method, and future studies to better quantify the influence of transported dust to overall DOD frequency distribution and incorporating station based surface wind records into the retrieval process will further improve the dataset.

866 *Data availability*. Both the monthly and annual mean $V_{threshold}$ data at a 0.5° by 0.5°
867 resolution in NetCDF format is archived at: https://www.gfdl.noaa.gov/pag-
868 homepage/
869
870 *Author contributions*. PG and BP conceived the study. PG processed the MODIS Deep
871 Blue aerosol data and guided model simulations. HG, SM, VN, ES, and MZ assisted with
872 model configurations, while CH, JK, BM, NO, CG, and JP provided guidance on data
873 usage and analysis. BP conducted model simulations, analyzed data and model results,
874 and wrote the paper with contributions from all other co-authors.
875
876 *Acknowledgements.*
877 This research is supported by NOAA and Princeton University's Cooperative
878 Institute for Climate Science and NASA under grant NNH14ZDA001N-ACMAP and
879 NNH16ZDA001N-MAP. The authors thank Drs. Veronica Chan and Hyeyum Shin for
880 their helpful comments on the early version of this paper and Dr. Sophie Vandenbussche
881 for her valuable suggestions. The helpful comments from two anonymous reviewers
882 improved the paper. We also thank the AERONET program for establishing and
883 maintaining the sunphotometer sites used in this study and the IMPROVE network for
884 the data. IMPROVE is a collaborative association of state, tribal, and federal agencies
885 and international partners. The US Environmental Protection Agency is the primary
886 funding source, with contracting and research support from the National Park Service.
887 The Air Quality Group at the University of California, Davis is the central analytical

888 laboratory, with ion analysis provided by Research Triangle Institute, and carbon analysis
889 provided by Desert Research Institute.
890 The AERONET aerosol optical depth data and SDA data are downloaded from
891 https://aeronet.gsfc.nasa.gov/new_web/download_all_v3_aod.html (last access: June
892 2018; Holben et al. 1998). IMPROVE fine dust data are downloaded from
893 http://views.cira.colostate.edu/fed/DataWizard/ (last access: March 2017, Malm et al.,
894 1994; Hand et al., 2011). MODIS LAI data may be requested by contacting Dr. Ranga
895 Myneni at Boston University.
896
897
898
899
900
901
902
903
904
905
906
907
908
909
910

911 Reference
912
913 Alfaro, S. C., and Gomes, L.: Modeling mineral aerosol production by wind erosion:
914 Emission intensities and aerosol size distributions in source areas, J Geophys Res-
915 Atmos, 106, 18075-18084, Doi 10.1029/2000jd900339, 2001.
916 Anderson, T. L., Wu, Y. H., Chu, D. A., Schmid, B., Redemann, J., and Dubovik, O.:
917 Testing the MODIS satellite retrieval of aerosol fine-mode fraction, J Geophys
918 Res-Atmos, 110, 10.1029/2005jd005978, 2005.
919 Andrews, E., Ogren, J. A., Kinne, S., and Samset, B.: Comparison of AOD, AAOD and
920 column single scattering albedo from AERONET retrievals and in situ profiling
921 measurements, Atmos Chem Phys, 17, 6041-6072, 10.5194/acp-17-6041-2017,
922 2017.
923 Baddock, M. C., Ginoux, P., Bullard, J. E., and Gill, T. E.: Do MODIS-defined dust
924 sources have a geomorphological signature?, Geophys Res Lett, 43, 2606-2613,
925 10.1002/2015gl067327, 2016.
926 Bangert, M., Nenes, A., Vogel, B., Vogel, H., Barahona, D., Karydis, V. A., Kumar, P.,
927 Kottmeier, C., and Blahak, U.: Saharan dust event impacts on cloud formation
928 and radiation over Western Europe, Atmos Chem Phys, 12, 4045-4063,
929 10.5194/acp-12-4045-2012, 2012.
930 Barchyn, T. E., and Hugenholtz, C. H.: Comparison of four methods to calculate aeolian
931 sediment transport threshold from field data: Implications for transport prediction
932 and discussion of method evolution, Geomorphology, 129, 190-203,
933 10.1016/j.geomorph.2011.01.022, 2011.

934 Bentsen, M., Bethke, I., Debernard, J. B., Iversen, T., Kirkevag, A., Seland, O., Drange,
935 H., Roelandt, C., Seierstad, I. A., Hoose, C., and Kristjansson, J. E.: The
936 Norwegian Earth System Model, NorESM1-M - Part 1: Description and basic
937 evaluation of the physical climate, Geosci Model Dev, 6, 687-720, 10.5194/gmd-
938 6-687-2013, 2013.
939 Bristow, C. S., Hudson-Edwards, K. A., and Chappell, A.: Fertilizing the Amazon and
940 equatorial Atlantic with West African dust, Geophys Res Lett, 37,
941 10.1029/2010gl043486, 2010.
942 Cheng, T., Peng, Y., Feichter, J., and Tegen, I.: An improvement on the dust emission
943 scheme in the global aerosol-climate model ECHAM5-HAM, Atmos Chem Phys,
944 8, 1105-1117, DOI 10.5194/acp-8-1105-2008, 2008.
945 Chomette, O., Legrand, M., and Marticorena, B.: Determination of the wind speed
946 threshold for the emission of desert dust using satellite remote sensing in the
947 thermal infrared, J Geophys Res-Atmos, 104, 31207-31215, Doi
948 10.1029/1999jd900756, 1999.
949 Collins, W. J., Bellouin, N., Doutriaux-Boucher, M., Gedney, N., Halloran, P., Hinton,
950 T., Hughes, J., Jones, C. D., Joshi, M., Liddicoat, S., Martin, G., O'Connor, F.,
951 Rae, J., Senior, C., Sitch, S., Totterdell, I., Wiltshire, A., and Woodward, S.:
952 Development and evaluation of an Earth-System model-HadGEM2, Geosci
953 Model Dev, 4, 1051-1075, 10.5194/gmd-4-1051-2011, 2011.
954 Cook, B. I., Miller, R. L., and Seager, R.: Dust and sea surface temperature forcing of the
955 1930s "Dust Bowl" drought, Geophys Res Lett, 35, 10.1029/2008gl033486, 2008.

956 Cook, B. I., Miller, R. L., and Seager, R.: Amplification of the North American "Dust
957 Bowl" drought through human-induced land degradation, P Natl Acad Sci USA,
958 106, 4997-5001, 10.1073/pnas.0810200106, 2009.
959 Cook, B. I., Seager, R., Miller, R. L., and Mason, J. A.: Intensification of North
960 American Megadroughts through Surface and Dust Aerosol Forcing, J Climate,
961 26, 4414-4430, 10.1175/Jcli-D-12-00022.1, 2013.
962 Cowie, S. M., Knippertz, P., and Marsham, J. H.: A climatology of dust emission events
963 from northern Africa using long-term surface observations, Atmos Chem Phys,
964 14, 8579-8597, 10.5194/acp-14-8579-2014, 2014.
965 Dee, D. P., Uppala, S. M., Simmons, A. J., Berrisford, P., Poli, P., Kobayashi, S., Andrae,
966 U., Balmaseda, M. A., Balsamo, G., Bauer, P., Bechtold, P., Beljaars, A. C. M.,
967 van de Berg, L., Bidlot, J., Bormann, N., Delsol, C., Dragani, R., Fuentes, M.,
968 Geer, A. J., Haimberger, L., Healy, S. B., Hersbach, H., Holm, E. V., Isaksen, L.,
969 Kallberg, P., Kohler, M., Matricardi, M., McNally, A. P., Monge-Sanz, B. M.,
970 Morcrette, J. J., Park, B. K., Peubey, C., de Rosnay, P., Tavolato, C., Thepaut, J.
971 N., and Vitart, F.: The ERA-Interim reanalysis: configuration and performance of
972 the data assimilation system, Q J Roy Meteor Soc, 137, 553-597, 10.1002/qj.828,
973 2011.
974 Donner, L. J., Wyman, B. L., Hemler, R. S., Horowitz, L. W., Ming, Y., Zhao, M., Golaz,
975 J. C., Ginoux, P., Lin, S. J., Schwarzkopf, M. D., Austin, J., Alaka, G., Cooke, W.
976 F., Delworth, T. L., Freidenreich, S. M., Gordon, C. T., Griffies, S. M., Held, I.
977 M., Hurlin, W. J., Klein, S. A., Knutson, T. R., Langenhorst, A. R., Lee, H. C.,
978 Lin, Y. L., Magi, B. I., Malyshev, S. L., Milly, P. C. D., Naik, V., Nath, M. J.,

Pincus, R., Ploshay, J. J., Ramaswamy, V., Seman, C. J., Shevliakova, E., Sirutis, J. J., Stern, W. F., Stouffer, R. J., Wilson, R. J., Winton, M., Wittenberg, A. T., and Zeng, F. R.: The Dynamical Core, Physical Parameterizations, and Basic Simulation Characteristics of the Atmospheric Component AM3 of the GFDL Global Coupled Model CM3, J Climate, 24, 3484-3519, 10.1175/2011jcli3955.1, 2011.

Draxier, R. R., and Hess, G. D.: An overview of the HYSPLIT_4 modelling system for trajectories, dispersion and deposition, Aust Meteorol Mag, 47, 295-308, 1998.

Draxler, R. R., Ginoux, P., and Stein, A. F.: An empirically derived emission algorithm for wind-blown dust, J Geophys Res-Atmos, 115, 10.1029/2009jd013167, 2010.

Du, J., Jones, L. A., and Kimball, J. S.: Daily Global Land Parameters Derived from AMSR-E and AMSR2, Version 2, https://doi.org/10.5067/RF8WPYOPJKL2, 2017a.

Du, J. Y., Kimball, J. S., Jones, L. A., Kim, Y., Glassy, J., and Watts, J. D.: A global satellite environmental data record derived from AMSR-E and AMSR2 microwave Earth observations, Earth Syst Sci Data, 9, 791-808, 10.5194/essd-9-791-2017, 2017b.

Dubovik, O., and King, M. D.: A flexible inversion algorithm for retrieval of aerosol optical properties from Sun and sky radiance measurements, J Geophys Res-Atmos, 105, 20673-20696, Doi 10.1029/2000jd900282, 2000.

Dumont, M., Brun, E., Picard, G., Michou, M., Libois, Q., Petit, J. R., Geyer, M., Morin, S., and Josse, B.: Contribution of light-absorbing impurities in snow to

1001 Greenland's darkening since 2009, Nat Geosci, 7, 509-512, 10.1038/Ngeo2180,
1002 2014.
1003 Dunion, J. P., and Velden, C. S.: The impact of the Saharan air layer on Atlantic tropical
1004 cyclone activity, B Am Meteorol Soc, 85, 353-+, 10.1175/Bams-85-3-353, 2004.
1005 Eck, T. F., Holben, B. N., Reid, J. S., Dubovik, O., Smirnov, A., O'Neill, N. T., Slutsker,
1006 I., and Kinne, S.: Wavelength dependence of the optical depth of biomass
1007 burning, urban, and desert dust aerosols, J Geophys Res-Atmos, 104, 31333-
1008 31349, Doi 10.1029/1999jd900923, 1999.
1009 Evan, A. T., Dunion, J., Foley, J. A., Heidinger, A. K., and Velden, C. S.: New evidence
1010 for a relationship between Atlantic tropical cyclone activity and African dust
1011 outbreaks, Geophys Res Lett, 33, 10.1029/2006gl026408, 2006.
1012 Evan, A. T., Fiedler, S., Zhao, C., Menut, L., Schepanski, K., Flamant, C., and Doherty,
1013 O.: Derivation of an observation-based map of North African dust emission,
1014 Aeolian Res, 16, 153-162, 10.1016/j.aeolia.2015.01.001, 2015.
1015 Evans, S., Ginoux, P., Malyshev, S., and Shevliakova, E.: Climate-vegetation interaction
1016 and amplification of Australian dust variability, Geophys Res Lett, 43, 11823-
1017 11830, 10.1002/2016gl071016, 2016.
1018 Fécan, F., Marticorena, B., and Bergametti, G.: Parametrization of the increase of the
1019 aeolian erosion threshold wind friction velocity due to soil moisture for arid and
1020 semi-arid areas, Ann Geophys-Atm Hydr, 17, 149-157, DOI
1021 10.1007/s005850050744, 1999.

1022 Fiedler, S., Kaplan, M. L., and Knippertz, P.: The importance of Harmattan surges for the
1023 emission of North African dust aerosol, Geophys Res Lett, 42, 9495-9504,
1024 10.1002/2015gl065925, 2015.
1025 Fung, I. Y., Meyn, S. K., Tegen, I., Doney, S. C., John, J. G., and Bishop, J. K. B.: Iron
1026 supply and demand in the upper ocean, Global Biogeochem Cy, 14, 281-295, Doi
1027 10.1029/1999gb900059, 2000.
1028 Garrigues, S., Lacaze, R., Baret, F., Morisette, J. T., Weiss, M., Nickeson, J. E.,
1029 Fernandes, R., Plummer, S., Shabanov, N. V., Myneni, R. B., Knyazikhin, Y., and
1030 Yang, W.: Validation and intercomparison of global Leaf Area Index products
1031 derived from remote sensing data, J Geophys Res-Biogeo, 113,
1032 10.1029/2007jg000635, 2008.
1033 Gillette, D. A., Adams, J., Endo, A., Smith, D., and Kihl, R.: Threshold Velocities for
1034 Input of Soil Particles into the Air by Desert Soils, J Geophys Res-Oceans, 85,
1035 5621-5630, 10.1029/JC085iC10p05621, 1980.
1036 Gillette, D. A., and Passi, R.: Modeling Dust Emission Caused by Wind Erosion, J
1037 Geophys Res-Atmos, 93, 14233-14242, DOI 10.1029/JD093iD11p14233, 1988.
1038 Ginoux, P., Chin, M., Tegen, I., Prospero, J. M., Holben, B., Dubovik, O., and Lin, S. J.:
1039 Sources and distributions of dust aerosols simulated with the GOCART model, J
1040 Geophys Res-Atmos, 106, 20255-20273, Doi 10.1029/2000jd000053, 2001.
1041 Ginoux, P., Horowitz, L. W., Ramaswamy, V., Geogdzhayev, I. V., Holben, B. N.,
1042 Stenchikov, G., and Tie, X.: Evaluation of aerosol distribution and optical depth
1043 in the Geophysical Fluid Dynamics Laboratory coupled model CM2.1 for present
1044 climate, J Geophys Res-Atmos, 111, 10.1029/2005jd006707, 2006.

1045 Ginoux, P., Garbuzov, D., and Hsu, N. C.: Identification of anthropogenic and natural
1046 dust sources using Moderate Resolution Imaging Spectroradiometer (MODIS)
1047 Deep Blue level 2 data, J Geophys Res-Atmos, 115, 10.1029/2009jd012398,
1048 2010.
1049 Ginoux, P., Prospero, J. M., Gill, T. E., Hsu, N. C., and Zhao, M.: Global-Scale
1050 Attribution of Anthropogenic and Natural Dust Sources and Their Emission Rates
1051 Based on MODIS Deep Blue Aerosol Products, Rev Geophys, 50,
1052 10.1029/2012rg000388, 2012.
1053 Ginoux, P., and Deroubaix, A.: Space observations of dust in East Asia, Air pollution in
1054 Eastern Asia: an integrated perspective, edited by: Bouarar, I., Wang, X., and
1055 Brasseur, G. P., Springer, 2017.
1056 Ginoux, P., Malyshev, S., Shevliakova, E., Chan, H. G., Guo, H., Milly, C., Naik, V.,
1057 Pascale, S., Paulot, F., Pu, B., Zhao, M., and Kapnick, S.: Distribution of
1058 absorbing aerosols in snow over high mountain ranges in GFDL AM4/LM4, in
1059 preparation, 2019.
1060 Hand, J. L., Copeland, S. A., Day, D. E., Dillner, A. M., Indresand, H., Malm, W. C.,
1061 McDade, C. E., Moore, C. T., Pitchford, M. L., Schichtel, B. A., and Watson, J.
1062 G.: IMPROVE (Interagency Monitoring of Protected Visual Environments):
1063 Spatial and seasonal patterns and temporal variability of haze and its constituents
1064 in the United States, 2011.
1065 Hand, J. L., White, W. H., Gebhart, K. A., Hyslop, N. P., Gill, T. E., and Schichtel, B. A.:
1066 Earlier onset of the spring fine dust season in the southwestern United States,
1067 Geophys Res Lett, 43, 4001-4009, 10.1002/2016gl068519, 2016.

1068 Hand, J. L., Gill, T. E., and Schichtel, B. A.: Spatial and seasonal variability in fine
1069 mineral dust and coarse aerosol mass at remote sites across the United States, J
1070 Geophys Res-Atmos, 122, 3080-3097, 10.1002/2016jd026290, 2017.
1071 Helgren, D. M., and Prospero, J. M.: Wind Velocities Associated with Dust Deflation
1072 Events in the Western Sahara, J Clim Appl Meteorol, 26, 1147-1151, Doi
1073 10.1175/1520-0450(1987)026<1147:Wvawdd>2.0.Co;2, 1987.
1074 Hersbach, H., and Dee, D.: ERA5 reanalysis is in production, ECMWF Newsletter, No.
1075 147, 7, 2016.
1076 Hoerling, M., Eischeid, J., Kumar, A., Leung, R., Mariotti, A., Mo, K., Schubert, S., and
1077 Seager, R.: Causes and Predictability of the 2012 Great Plains Drought, B Am
1078 Meteorol Soc, 95, 269-282, 10.1175/Bams-D-13-00055.1, 2014.
1079 Holben, B. N., Eck, T. F., Slutsker, I., Tanre, D., Buis, J. P., Setzer, A., Vermote, E.,
1080 Reagan, J. A., Kaufman, Y. J., Nakajima, T., Lavenu, F., Jankowiak, I., and
1081 Smirnov, A.: AERONET - A federated instrument network and data archive for
1082 aerosol characterization, Remote Sens Environ, 66, 1-16, Doi 10.1016/S0034-
1083 4257(98)00031-5, 1998.
1084 Holben, B. N., Eck, T. F., Slutsker, I., Smirnov, A., Sinyuk, A., Schafer, J., Giles, D., and
1085 Dubovik, O.: AERONET's Version 2.0 quality assurance criteria, 2006.
1086 Hsu, N. C., Tsay, S. C., King, M. D., and Herman, J. R.: Aerosol properties over bright-
1087 reflecting source regions, Ieee T Geosci Remote, 42, 557-569,
1088 10.1109/Tgrs.2004.824067, 2004.
1089 Hsu, N. C., Jeong, M. J., Bettenhausen, C., Sayer, A. M., Hansell, R., Seftor, C. S.,
1090 Huang, J., and Tsay, S. C.: Enhanced Deep Blue aerosol retrieval algorithm: The

second generation, J Geophys Res-Atmos, 118, 9296-9315, 10.1002/jgrd.50712, 2013.

Huneeus, N., Schulz, M., Balkanski, Y., Griesfeller, J., Prospero, J., Kinne, S., Bauer, S., Boucher, O., Chin, M., Dentener, F., Diehl, T., Easter, R., Fillmore, D., Ghan, S., Ginoux, P., Grini, A., Horowitz, L., Koch, D., Krol, M. C., Landing, W., Liu, X., Mahowald, N., Miller, R., Morcrette, J. J., Myhre, G., Penner, J., Perlwitz, J., Stier, P., Takemura, T., and Zender, C. S.: Global dust model intercomparison in AeroCom phase I, Atmos Chem Phys, 11, 7781-7816, 10.5194/acp-11-7781-2011, 2011.

Jickells, T. D., An, Z. S., Andersen, K. K., Baker, A. R., Bergametti, G., Brooks, N., Cao, J. J., Boyd, P. W., Duce, R. A., Hunter, K. A., Kawahata, H., Kubilay, N., laRoche, J., Liss, P. S., Mahowald, N., Prospero, J. M., Ridgwell, A. J., Tegen, I., and Torres, R.: Global iron connections between desert dust, ocean biogeochemistry, and climate, Science, 308, 67-71, DOI 10.1126/science.1105959, 2005.

Jin, Q., Wei, J., Yang, Z. L., Pu, B., and Huang, J.: Consistent response of Indian summer monsoon to Middle East dust in observations and simulations, Atmos Chem Phys, 15, 9897-9915, 10.5194/acp-15-9897-2015, 2015.

Jin, Q. J., Wei, J. F., and Yang, Z. L.: Positive response of Indian summer rainfall to Middle East dust, Geophys Res Lett, 41, 4068-4074, 10.1002/2014gl059980, 2014.

1112 Jin, Q. J., Yang, Z. L., and Wei, J. F.: Seasonal Responses of Indian Summer Monsoon to
1113 Dust Aerosols in the Middle East, India, and China, J Climate, 29, 6329-6349,
1114 10.1175/Jcli-D-15-0622.1, 2016.
1115 Jones, C. D., Hughes, J. K., Bellouin, N., Hardiman, S. C., Jones, G. S., Knight, J.,
1116 Liddicoat, S., O'Connor, F. M., Andres, R. J., Bell, C., Boo, K. O., Bozzo, A.,
1117 Butchart, N., Cadule, P., Corbin, K. D., Doutriaux-Boucher, M., Friedlingstein,
1118 P., Gornall, J., Gray, L., Halloran, P. R., Hurtt, G., Ingram, W. J., Lamarque, J. F.,
1119 Law, R. M., Meinshausen, M., Osprey, S., Palin, E. J., Chini, L. P., Raddatz, T.,
1120 Sanderson, M. G., Sellar, A. A., Schurer, A., Valdes, P., Wood, N., Woodward,
1121 S., Yoshioka, M., and Zerroukat, M.: The HadGEM2-ES implementation of
1122 CMIP5 centennial simulations, Geosci Model Dev, 4, 543-570, 10.5194/gmd-4-
1123 543-2011, 2011.
1124 Kalnay, E., Kanamitsu, M., Kistler, R., Collins, W., Deaven, D., Gandin, L., Iredell, M.,
1125 Saha, S., White, G., Woollen, J., Zhu, Y., Chelliah, M., Ebisuzaki, W., Higgins,
1126 W., Janowiak, J., Mo, K. C., Ropelewski, C., Wang, J., Leetmaa, A., Reynolds,
1127 R., Jenne, R., and Joseph, D.: The NCEP/NCAR 40-year reanalysis project, B Am
1128 Meteorol Soc, 77, 437-471, Doi 10.1175/1520-
1129 0477(1996)077<0437:Tnyrp>2.0.Co;2, 1996.
1130 Kim, D., Chin, M. A., Bian, H. S., Tan, Q., Brown, M. E., Zheng, T., You, R. J., Diehl,
1131 T., Ginoux, P., and Kucsera, T.: The effect of the dynamic surface bareness on
1132 dust source function, emission, and distribution, J Geophys Res-Atmos, 118, 871-
1133 886, 10.1029/2012jd017907, 2013.

1134 Kim, M. K., Lau, W. K. M., Kim, K. M., Sang, J., Kim, Y. H., and Lee, W. S.:
1135 Amplification of ENSO effects on Indian summer monsoon by absorbing
1136 aerosols, Clim Dynam, 46, 2657-2671, 10.1007/s00382-015-2722-y, 2016.
1137 Knippertz, P.: Dust emissions in the West African heat trough - the role of the diurnal
1138 cycle and of extratropical disturbances, Meteorol Z, 17, 553-563, 10.1127/0941-
1139 2948/2008/0315, 2008.
1140 Kok, J. F., Albani, S., Mahowald, N. M., and Ward, D. S.: An improved dust emission
1141 model - Part 2: Evaluation in the Community Earth System Model, with
1142 implications for the use of dust source functions, Atmos Chem Phys, 14, 13043-
1143 13061, 10.5194/acp-14-13043-2014, 2014a.
1144 Kok, J. F., Mahowald, N. M., Fratini, G., Gillies, J. A., Ishizuka, M., Leys, J. F., Mikami,
1145 M., Park, M. S., Park, S. U., Van Pelt, R. S., and Zobeck, T. M.: An improved
1146 dust emission model - Part 1: Model description and comparison against
1147 measurements, Atmos Chem Phys, 14, 13023-13041, 10.5194/acp-14-13023-
1148 2014, 2014b.
1149 Kurosaki, Y., and Mikami, M.: Effect of snow cover on threshold wind velocity of dust
1150 outbreak, Geophys Res Lett, 31, 10.1029/2003gl018632, 2004.
1151 Kurosaki, Y., and Mikami, M.: Threshold wind speed for dust emission in east Asia and
1152 its seasonal variations, J Geophys Res-Atmos, 112, 10.1029/2006jd007988, 2007.
1153 Largeron, Y., Guichard, F., Bouniol, D., Couvreux, F., Kergoat, L., and Marticorena, B.:
1154 Can we use surface wind fields from meteorological reanalyses for Sahelian dust
1155 emission simulations?, Geophys Res Lett, 42, 2490-2499, 10.1002/2014gl062938,
1156 2015.

1157 Levin, Z., Ganor, E., and Gladstein, V.: The effects of desert particles coated with sulfate
1158 on rain formation in the eastern Mediterranean, J Appl Meteorol, 35, 1511-1523,
1159 Doi 10.1175/1520-0450(1996)035<1511:Teodpc>2.0.Co;2, 1996.
1160 Lin, C. Y., Zhao, C., Liu, X. H., Lin, N. H., and Chen, W. N.: Modelling of long-range
1161 transport of Southeast Asia biomass-burning aerosols to Taiwan and their
1162 radiative forcings over East Asia, Tellus B, 66, 10.3402/tellusb.v66.23733, 2014.
1163 Mahowald, N. M., Baker, A. R., Bergametti, G., Brooks, N., Duce, R. A., Jickells, T. D.,
1164 Kubilay, N., Prospero, J. M., and Tegen, I.: Atmospheric global dust cycle and
1165 iron inputs to the ocean, Global Biogeochem Cy, 19, 10.1029/2004gb002402,
1166 2005.
1167 Mahowald, N. M., Kloster, S., Engelstaedter, S., Moore, J. K., Mukhopadhyay, S.,
1168 McConnell, J. R., Albani, S., Doney, S. C., Bhattacharya, A., Curran, M. A. J.,
1169 Flanner, M. G., Hoffman, F. M., Lawrence, D. M., Lindsay, K., Mayewski, P. A.,
1170 Neff, J., Rothenberg, D., Thomas, E., Thornton, P. E., and Zender, C. S.:
1171 Observed 20th century desert dust variability: impact on climate and
1172 biogeochemistry, Atmos Chem Phys, 10, 10875-10893, 10.5194/acp-10-10875-
1173 2010, 2010.
1174 Malm, W. C., Sisler, J. F., Huffman, D., Eldred, R. A., and Cahill, T. A.: Spatial and
1175 Seasonal Trends in Particle Concentration and Optical Extinction in the United-
1176 States, J Geophys Res-Atmos, 99, 1347-1370, Doi 10.1029/93jd02916, 1994.
1177 Marsham, J. H., Hobby, M., Allen, C. J. T., Banks, J. R., Bart, M., Brooks, B. J.,
1178 Cavazos-Guerra, C., Engelstaedter, S., Gascoyne, M., Lima, A. R., Martins, J. V.,
1179 McQuaid, J. B., O'Leary, A., Ouchene, B., Ouladichir, A., Parker, D. J., Saci, A.,

1180 Salah-Ferroudj, M., Todd, M. C., and Washington, R.: Meteorology and dust in
1181 the central Sahara: Observations from Fennec supersite-1 during the June 2011
1182 Intensive Observation Period, J Geophys Res-Atmos, 118, 4069-4089,
1183 10.1002/jgrd.50211, 2013.
1184 Marticorena, B., and Bergametti, G.: Modeling the Atmospheric Dust Cycle .1. Design of
1185 a Soil-Derived Dust Emission Scheme, J Geophys Res-Atmos, 100, 16415-16430,
1186 Doi 10.1029/95jd00690, 1995.
1187 Marticorena, B., Bergametti, G., Aumont, B., Callot, Y., NDoume, C., and Legrand, M.:
1188 Modeling the atmospheric dust cycle .2. Simulation of Saharan dust sources, J
1189 Geophys Res-Atmos, 102, 4387-4404, Doi 10.1029/96jd02964, 1997.
1190 Marticorena, B., Chatenet, B., Rajot, J. L., Traore, S., Coulibaly, M., Diallo, A., Kone, I.,
1191 Maman, A., Diaye, T. N., and Zakou, A.: Temporal variability of mineral dust
1192 concentrations over West Africa: analyses of a pluriannual monitoring from the
1193 AMMA Sahelian Dust Transect, Atmos Chem Phys, 10, 8899-8915, 10.5194/acp-
1194 10-8899-2010, 2010.
1195 Mbourou, G. N., Bertrand, J. J., and Nicholson, S. E.: The diurnal and seasonal cycles of
1196 wind-borne dust over Africa north of the equator, J Appl Meteorol, 36, 868-882,
1197 Doi 10.1175/1520-0450(1997)036<0868:Tdasco>2.0.Co;2, 1997.
1198 Miller, R. L., and Tegen, I.: Climate response to soil dust aerosols, J Climate, 11, 3247-
1199 3267, Doi 10.1175/1520-0442(1998)011<3247:Crtsda>2.0.Co;2, 1998.
1200 Miller, R. L., Tegen, I., and Perlwitz, J.: Surface radiative forcing by soil dust aerosols
1201 and the hydrologic cycle, J Geophys Res-Atmos, 109, 10.1029/2003jd004085,
1202 2004.

1203 Moorthi, S., and Suarez, M. J.: Relaxed Arakawa-Schubert - a Parameterization of Moist
1204 Convection for General-Circulation Models, Mon Weather Rev, 120, 978-1002,
1205 Doi 10.1175/1520-0493(1992)120<0978:Rasapo>2.0.Co;2, 1992.
1206 Naik, V., Horowitz, L. W., Fiore, A. M., Ginoux, P., Mao, J. Q., Aghedo, A. M., and
1207 Levy, H.: Impact of preindustrial to present-day changes in short-lived pollutant
1208 emissions on atmospheric composition and climate forcing, J Geophys Res-
1209 Atmos, 118, 8086-8110, 10.1002/jgrd.50608, 2013.
1210 Nakajima, T., Higurashi, A., Kawamoto, K., and Penner, J. E.: A possible correlation
1211 between satellite-derived cloud and aerosol microphysical parameters, Geophys
1212 Res Lett, 28, 1171-1174, Doi 10.1029/2000gl012186, 2001.
1213 O'Neill, N. T., Eck, T. F., Smirnov, A., Holben, B. N., and Thulasiraman, S.: Spectral
1214 discrimination of coarse and fine mode optical depth, J Geophys Res-Atmos, 108,
1215 10.1029/2002jd002975, 2003.
1216 O'rgill, M., and Sehmel, G.: Frequency and diurnal variation of dust storms in the
1217 contiguous U.S.A., Atmospheric Environment, 10, 813-825, 1976.
1218 Painter, T. H., Deems, J. S., Belnap, J., Hamlet, A. F., Landry, C. C., and Udall, B.:
1219 Response of Colorado River runoff to dust radiative forcing in snow, P Natl Acad
1220 Sci USA, 107, 17125-17130, 10.1073/pnas.0913139107, 2010.
1221 Painter, T. H., Skiles, S. M., Deems, J. S., Brandt, W. T., and Dozier, J.: Variation in
1222 Rising Limb of Colorado River Snowmelt Runoff Hydrograph Controlled by Dust
1223 Radiative Forcing in Snow, Geophys Res Lett, 45, 797-808,
1224 10.1002/2017gl075826, 2018.

1225 Pu, B., and Ginoux, P.: The impact of the Pacific Decadal Oscillation on springtime dust
1226 activity in Syria, Atmos Chem Phys, 16, 13431-13448, 10.5194/acp-16-13431-
1227 2016, 2016.
1228 Pu, B., and Ginoux, P.: Projection of American dustiness in the late 21st century due to
1229 climate change, Scientific reports, 7, 10.1038/s41598-017-05431-9, 2017.
1230 Pu, B., and Ginoux, P.: Climatic factors contributing to long-term variations in surface
1231 fine dust concentration in the United States, Atmos Chem Phys, 18, 4201-4215,
1232 10.5194/acp-18-4201-2018, 2018a.
1233 Pu, B., and Ginoux, P.: How reliable are CMIP5 models in simulating dust optical
1234 depth?, Atmos Chem Phys, 18, 12491-12510, 10.5194/acp-18-12491-2018,
1235 2018b.
1236 Putman, W. M., and Lin, S. H.: Finite-volume transport on various cubed-sphere grids, J
1237 Comput Phys, 227, 55-78, 10.1016/j.jcp.2007.07.022, 2007.
1238 Raupach, M. R., Gillette, D. A., and Leys, J. F.: The Effect of Roughness Elements on
1239 Wind Erosion Threshold, J Geophys Res-Atmos, 98, 3023-3029, Doi
1240 10.1029/92jd01922, 1993.
1241 Rayner, N. A., Parker, D. E., Horton, E. B., Folland, C. K., Alexander, L. V., Rowell, D.
1242 P., Kent, E. C., and Kaplan, A.: Global analyses of sea surface temperature, sea
1243 ice, and night marine air temperature since the late nineteenth century, J Geophys
1244 Res-Atmos, 108, 10.1029/2002jd002670, 2003.
1245 Reid, J. S., Hyer, E. J., Prins, E. M., Westphal, D. L., Zhang, J. L., Wang, J., Christopher,
1246 S. A., Curtis, C. A., Schmidt, C. C., Eleuterio, D. P., Richardson, K. A., and
1247 Hoffman, J. P.: Global Monitoring and Forecasting of Biomass-Burning Smoke:

1248 Description of and Lessons From the Fire Locating and Modeling of Burning
1249 Emissions (FLAMBE) Program, Ieee J-Stars, 2, 144-162,
1250 10.1109/Jstars.2009.2027443, 2009.
1251 Reynolds, R. W., Rayner, N. A., Smith, T. M., Stokes, D. C., and Wang, W. Q.: An
1252 improved in situ and satellite SST analysis for climate, J Climate, 15, 1609-1625,
1253 Doi 10.1175/1520-0442(2002)015<1609:Aiisas>2.0.Co;2, 2002.
1254 Rieger, D., Steiner, A., Bachmann, V., Gasch, P., Forstner, J., Deetz, K., Vogel, B., and
1255 Vogel, H.: Impact of the 4 April 2014 Saharan dust outbreak on the photovoltaic
1256 power generation in Germany, Atmos Chem Phys, 17, 13391-13415,
1257 10.5194/acp-17-13391-2017, 2017.
1258 Rienecker, M. M., Suarez, M. J., Todling, R., Bacmeister, J., Takacs, L., Liu, H.-C., Gu,
1259 W., Sienkiewicz, M., Koster, R. D., Gelaro, R., Stajner, I., and Nielsen, J. E.: The
1260 GEOS‐5 Data Assimilation System−Documentation of versions 5.0.1, 5.1.0, and
1261 5.2.0, Technical Report Series on Global Modeling and Data Assimilation, 27
1262 (available at http://gmao.gsfc.nasa.gov/pubs/docs/Rienecker369.pdf), 2008.
1263 Rosenfield, J. E., Considine, D. B., Meade, P. E., Bacmeister, J. T., Jackman, C. H., and
1264 Schoeberl, M. R.: Stratospheric effects of Mount Pinatubo aerosol studied with a
1265 coupled two-dimensional model, J Geophys Res-Atmos, 102, 3649-3670, Doi
1266 10.1029/96jd03820, 1997.
1267 Savoie, D. L., and Prospero, J. M.: Comparison of Oceanic and Continental Sources of
1268 Non-Sea-Salt Sulfate over the Pacific-Ocean, Nature, 339, 685-687, DOI
1269 10.1038/339685a0, 1989.

1270 Sayer, A. M., Hsu, N. C., Bettenhausen, C., and Jeong, M. J.: Validation and uncertainty
1271 estimates for MODIS Collection 6 "Deep Blue" aerosol data, J Geophys Res-
1272 Atmos, 118, 7864-7872, 10.1002/jgrd.50600, 2013.
1273 Schepanski, K., Tegen, I., Laurent, B., Heinold, B., and Macke, A.: A new Saharan dust
1274 source activation frequency map derived from MSG-SEVIRI IR-channels,
1275 Geophys Res Lett, 34, 10.1029/2007gl030168, 2007.
1276 Schepanski, K., Tegen, I., Todd, M. C., Heinold, B., Bonisch, G., Laurent, B., and
1277 Macke, A.: Meteorological processes forcing Saharan dust emission inferred from
1278 MSG-SEVIRI observations of subdaily dust source activation and numerical
1279 models, J Geophys Res-Atmos, 114, 10.1029/2008jd010325, 2009.
1280 Shao, Y.: A model for mineral dust emission, J Geophys Res-Atmos, 106, 20239-20254,
1281 Doi 10.1029/2001jd900171, 2001.
1282 Shao, Y. P., Wyrwoll, K. H., Chappell, A., Huang, J. P., Lin, Z. H., McTainsh, G. H.,
1283 Mikami, M., Tanaka, T. Y., Wang, X. L., and Yoon, S.: Dust cycle: An emerging
1284 core theme in Earth system science, Aeolian Res, 2, 181-204,
1285 10.1016/j.aeolia.2011.02.001, 2011.
1286 Sharma, D., and Miller, R. L.: Revisiting the observed correlation between weekly
1287 averaged Indian monsoon precipitation and Arabian Sea aerosol optical depth,
1288 Geophys Res Lett, 44, 10006-10016, 10.1002/2017gl074373, 2017.
1289 Solmon, F., Nair, V. S., and Mallet, M.: Increasing Arabian dust activity and the Indian
1290 summer monsoon, Atmos Chem Phys, 15, 8051-8064, 10.5194/acp-15-8051-
1291 2015, 2015.

Strong, J. D., Vecchi, G. A., and Ginoux, P.: The Climatological Effect of Saharan Dust on Global Tropical Cyclones in a Fully Coupled GCM, Journal of Geophysical Research - Atmospheres, 123, https://doi.org/10.1029/2017JD027808, 2018.

Strong, J. D. O., Vecchi, G. A., and Ginoux, P.: The Response of the Tropical Atlantic and West African Climate to Saharan Dust in a Fully Coupled GCM, J Climate, 28, 7071-7092, 10.1175/Jcli-D-14-00797.1, 2015.

Takemura, T., Okamoto, H., Maruyama, Y., Numaguti, A., Higurashi, A., and Nakajima, T.: Global three-dimensional simulation of aerosol optical thickness distribution of various origins, J Geophys Res-Atmos, 105, 17853-17873, Doi 10.1029/2000jd900265, 2000.

Taylor, K., Williamson, D., and Zwiers, F.: The sea surface temperature and sea ice concentration boundary conditions for AMIP II simulations (PCMDI Rep. 60, pp. 1–25), Livermore, CA:Program for Climate Model Diagnosis and Intercomparison, Lawrence Livermore National Laboratory, 2000.

Tegen, I., and Fung, I.: Modeling of Mineral Dust in the Atmosphere - Sources, Transport, and Optical-Thickness, J Geophys Res-Atmos, 99, 22897-22914, Doi 10.1029/94jd01928, 1994.

Tong, D. Q., Wang, J. X. L., Gill, T. E., Lei, H., and Wang, B. Y.: Intensified dust storm activity and Valley fever infection in the southwestern United States, Geophys Res Lett, 44, 4304-4312, 10.1002/2017gl073524, 2017.

Uno, I., Amano, H., Emori, S., Kinoshita, K., Matsui, I., and Sugimoto, N.: Trans-Pacific yellow sand transport observed in April 1998: A numerical simulation, J Geophys Res-Atmos, 106, 18331-18344, Doi 10.1029/2000jd900748, 2001.

1315 Vinoj, V., Rasch, P. J., Wang, H. L., Yoon, J. H., Ma, P. L., Landu, K., and Singh, B.:
1316 Short-term modulation of Indian summer monsoon rainfall by West Asian dust,
1317 Nat Geosci, 7, 308-313, 10.1038/ngeo2107, 2014.
1318 Watanabe, S., Hajima, T., Sudo, K., Nagashima, T., Takemura, T., Okajima, H., Nozawa,
1319 T., Kawase, H., Abe, M., Yokohata, T., Ise, T., Sato, H., Kato, E., Takata, K.,
1320 Emori, S., and Kawamiya, M.: MIROC-ESM 2010: model description and basic
1321 results of CMIP5-20c3m experiments, Geosci Model Dev, 4, 845-872,
1322 10.5194/gmd-4-845-2011, 2011.
1323 Westphal, D. L., Curtis, C. A., Liu, M., and Walker, A. L.: Operational aerosol and dust
1324 storm forecasting, in WMO/GEO Expert Meeting on an International Sand and
1325 Dust Storm Warning System, IOP Conference Series Earth and Environmental
1326 Science, 2009.
1327 Winker, D. M., Hunt, W., and Hostetler, C.: Status and performance of the CALIOP
1328 lidar, Bba Lib, 5575, 8-15, 10.1117/12.571955, 2004.
1329 Winker, D. M., Hunt, W. H., and McGill, M. J.: Initial performance assessment of
1330 CALIOP, Geophys Res Lett, 34, 10.1029/2007gl030135, 2007.
1331 Witek, M. L., Flatau, P. J., Quinn, P. K., and Westphal, D. L.: Global sea-salt modeling:
1332 Results and validation against multicampaign shipboard measurements, J
1333 Geophys Res-Atmos, 112, 10.1029/2006jd007779, 2007.
1334 Wong, S., and Dessler, A. E.: Suppression of deep convection over the tropical North
1335 Atlantic by the Saharan Air Layer, Geophys Res Lett, 32, 10.1029/2004gl022295,
1336 2005.

Wurzler, S., Reisin, T. G., and Levin, Z.: Modification of mineral dust particles by cloud processing and subsequent effects on drop size distributions, J Geophys Res-Atmos, 105, 4501-4512, Doi 10.1029/1999jd900980, 2000.

Yan, K., Park, T., Yan, G. J., Chen, C., Yang, B., Liu, Z., Nemani, R. R., Knyazikhin, Y., and Myneni, R. B.: Evaluation of MODIS LAI/FPAR Product Collection 6. Part 1: Consistency and Improvements, Remote Sens-Basel, 8, 10.3390/rs8050359, 2016a.

Yan, K., Park, T., Yan, G. J., Liu, Z., Yang, B., Chen, C., Nemani, R. R., Knyazikhin, Y., and Myneni, R. B.: Evaluation of MODIS LAI/FPAR Product Collection 6. Part 2: Validation and Intercomparison, Remote Sens-Basel, 8, 10.3390/rs8060460, 2016b.

Yu, H. B., Chin, M., Yuan, T. L., Bian, H. S., Remer, L. A., Prospero, J. M., Omar, A., Winker, D., Yang, Y. K., Zhang, Y., Zhang, Z. B., and Zhao, C.: The fertilizing role of African dust in the Amazon rainforest: A first multiyear assessment based on data from Cloud-Aerosol Lidar and Infrared Pathfinder Satellite Observations, Geophys Res Lett, 42, 1984-1991, 10.1002/2015gl063040, 2015.

Zender, C. S., Bian, H. S., and Newman, D.: Mineral Dust Entrainment and Deposition (DEAD) model: Description and 1990s dust climatology, J Geophys Res-Atmos, 108, 10.1029/2002jd002775, 2003.

Zhao, M., Golaz, J. C., Held, I. M., Guo, H., Balaji, V., Benson, R., Chen, J. H., Chen, X., Donner, L. J., Dunne, J. P., Dunne, K., Durachta, J., Fan, S. M., Freidenreich, S. M., Garner, S. T., Ginoux, P., Harris, L. M., Horowitz, L. W., Krasting, J. P., Langenhorst, A. R., Liang, Z., Lin, P., Lin, S. J., Malyshev, S. L., Mason, E.,

Milly, P. C. D., Ming, Y., Naik, V., Paulot, F., Paynter, D., Phillipps, P., Radhakrishnan, A., Ramaswamy, V., Robinson, T., Schwarzkopf, D., Seman, C. J., Shevliakova, E., Shen, Z., Shin, H., Silvers, L. G., Wilson, J. R., Winton, M., Wittenberg, A. T., Wyman, B., and Xiang, B.: The GFDL Global Atmosphere and Land Model AM4.0/LM4.0:1. Simulation Characteristics With Prescribed SSTs, J Adv Model Earth Sy, 10, 691-734, 10.1002/2017ms001208, 2018a.

Zhao, M., Golaz, J. C., Held, I. M., Guo, H., Balaji, V., Benson, R., Chen, J. H., Chen, X., Donner, L. J., Dunne, J. P., Dunne, K., Durachta, J., Fan, S. M., Freidenreich, S. M., Garner, S. T., Ginoux, P., Harris, L. M., Horowitz, L. W., Krasting, J. P., Langenhorst, A. R., Liang, Z., Lin, P., Lin, S. J., Malyshev, S. L., Mason, E., Milly, P. C. D., Ming, Y., Naik, V., Paulot, F., Paynter, D., Phillipps, P., Radhakrishnan, A., Ramaswamy, V., Robinson, T., Schwarzkopf, D., Seman, C. J., Shevliakova, E., Shen, Z., Shin, H., Silvers, L. G., Wilson, J. R., Winton, M., Wittenberg, A. T., Wyman, B., and Xiang, B.: The GFDL Global Atmosphere and Land Model AM4.0/LM4.0:2. Model Description, Sensitivity Studies, and Tuning Strategies, J Adv Model Earth Sy, 10, 735-769, 10.1002/2017ms001209, 2018b.

1377 Table 1 Major dust source regions shown in Figure 1. Note that region names such as
1378 India and northern China are not exactly the same as their geographical definitions but
1379 also cover some areas from nearby countries.
1380
1381 Table 2 Sensitivity of annual mean wind erosion threshold (m s^{-1}) to the selection of
1382 different retrieval criteria. Note the setting of the last column is the same as
1383 DOD_{thresh}=0.2 or 0.02, except surface DOD (sDOD) from Aqua is used over North
1384 Africa.
1385
1386 Table 3 Sensitivity of annual mean wind erosion threshold (m s^{-1}) to surface wind speeds
1387 from different reanalyses (DOD_{thresh}= 0.2 or 0.02).
1388
1389 Table 4 Simulation design
1390
1391
1392
1393
1394
1395
1396
1397
1398
1399

Figure 1. (a)-(e) Frequencies of occurrence (FoO; unit: days per season) in each season and annual mean. (f)-(j) Threshold of wind erosion ($V_{threshold}$; unit: m s^{-1}) derived from satellite products and reanalyses for each season and annual mean using DOD_{thresh}=0.2 (or 0.02). Black boxes in (f) denote nine dust source regions as listed in Table 1.

Figure 2. (a)-(i) Frequency distribution of annual mean $V_{threshold}$ (black bars) in each region (black boxes in Fig. 1) and for dusty seasons, i.e., MAM (green) and JJA (blue) for regions in the Northern Hemisphere and SON (orange) and DJF (grey) for regions in the Southern Hemisphere. The mean (averaged over all grid points in the region, without area weight) and ± one standard deviations of $V_{threshold}$ in each region are shown on the top right of each plot.

Figure 3. (a)-(e) Threshold of wind erosion ($V_{threshold}$; unit: m s^{-1}) derived from satellite products and reanalyses for each season and annual mean using DOD_{thresh}=0.5 (or 0.05). Black boxes in (a) denote nine dust source regions as listed in Table 1.

Figure 4. Climatology of annual mean AERONET (a) AOD (550 nm) and (b) SDA COD (500 nm) averaged over 2003-2015.

Figure 5. Scatter plot of simulated annual mean (a) AOD and (b) COD in the Control run versus AERONET AOD and COD (left), and the relative difference (in percentage) (c) between modeled AOD and AERONET AOD and (d) between modeled COD and AERONET COD (right). (e) The relative contribution of DOD to COD in the model.

1423 Figure 6. Same as Fig. 5 but for the V_{thresh}12mn simulation.

1424

1425 Figure 7. (a) Climatology (2003-2015) of AERONET DOD (550 nm) over major dusty
1426 regions and (b) scatter plot of modeled DOD in the V_{thresh}12mn simulation versus
1427 AERONET DOD, and (c) the relative difference (in percentage) between modeled DOD
1428 and AERONET DOD in the V_{thresh}12mn simulation.

1429

1430 Figure 8. Regional averaged annual mean DOD (2003-2015) over nine regions from the
1431 Control (grey), V_{thresh}12mn (orange), and V_{thresh}Ann (yellow) simulations and MODIS
1432 (black).

1433

1434 Figure 9. Scatter plots (left column) of model simulated (from top to bottom are the
1435 Control, V_{thresh}Ann, and V_{thresh}12mn simulations) surface dust concentration versus the
1436 climatology of observed surface dust concentration from RSMAS stations (Savoie and
1437 Prospero 1989), and spatial pattern of surface dust concentration from model output
1438 (shading; right column) and the ratio between modeled and RSMAS station observed
1439 surface dust concentration (color triangles, with upward triangles indicating
1440 overestimation and downward triangles indicating underestimation). 16 stations were
1441 used, and numbers in each triangle (right) and grey dots (left) indicate the stations. The
1442 one-one, one-two and one-five lines are plotted in solid, dashed and dash-dotted lines in
1443 the scatter plots. Statistics in the scatter plots are calculated in logarithmic space.

1444

1445 Figure 10. Annual mean surface fine dust concentration (μg m^{-3}) from IMPROVE
1446 stations (left column) and three simulations (middle column) and the differences between
1447 model and observation (right column) for 2002-2015.
1448
1449 Figure 11. Seasonal cycle of DOD from MODIS (black), the Control (grey), V_{thresh}12mn
1450 (orange), and V_{thresh}Ann (yellow) runs, and gridded AERONET SDA COD (blue)
1451 averaged over nine regions. The annual mean of each dataset in each region is listed on
1452 the top of the plot.
1453
1454 Figure 12. Seasonal cycle of DOD over 12 AERONET SDA sites (see Fig. S7 in the
1455 Supplement for locations) from the Control (grey), V_{thresh}12mn (orange), and V_{thresh}Ann
1456 (yellow) simulations, along with DOD from MODIS (blue), and COD from AERONET
1457 (black dotted line). All values are averaged over 2003-2015. The location (lat/long) and
1458 the name (due to space, only first seven characters are shown) of the sites are listed at the
1459 top of each plot.
1460
1461 Figure 13. (a)-(c) Seasonal cycle of PM_{10} surface concentration (black) over three sites
1462 from the LISA project, along with PM_{10} surface dust concentration from the Control
1463 (grey), V_{thresh}12mn (orange), and V_{thresh}Ann (yellow) simulations. Error bars are ± one
1464 standard deviations of daily mean in each month averaged over 2006-2014. Unites: μg m^{-3}.
1465 (d)-(f) seasonal cycle of DOD (550 nm) from three AERONET sites co-located with
1466 LISA sites (blue) versus that modeled by the Control (grey), V_{thresh}12mn (orange), and
1467 V_{thresh}Ann (yellow) simulations.

Figure 14. Daily DOD from MODIS (top panel), daily DOD simulated by the V_{thresh}12mn run along with anomalies (with reference to the 2000-2015 mean) of surface wind vectors (m s^{-1}; bottom panel) from Oct. 17th to Oct. 19th, 2012. Only DOD over land is shown. Missing values in MODIS DOD (top panel) are plotted in grey shading.

Figure 15. Frequency (%) distribution of regional averaged daily DOD from MODIS (black) versus that from the Control (light blue) and V_{thresh}12mn (orange) simulations for the Sahara, the Sahel, the Arabian Peninsula, northern China, India, western to central U.S., South America, South Africa, and Australia from 2003 to 2015. X-axis denotes the ranges of DOD (the bin spacing for dusty regions is 0.05 and for less dusty regions is 0.01), and y-axis is percentage of occurrence. The light green boxes denote the averaging areas. For regions in the Northern Hemisphere frequency in MAM is shown, while for regions in the Southern Hemisphere frequency in SON is shown.

Table 1 Major dust source regions shown in Figure 1. Note that region names such as India and northern China are not exactly the same as their geographical definitions but also cover some areas from nearby countries.

No.	Regions	Lat/long
1	Sahel	10°-20°N, 18°W-35°E
2	Sahara	20°-35°N, 15°W-25°E
3	Arabian Peninsula	15°-35°N, 35°-60°E
4	Northern China (N. China)	35°-45°N, 77°-103°E
5	India	20°-35°N, 60°-85°E
6	U.S.	25°-45°N, 102°-125°W
7	South Africa (S. Africa)	17°-35°S, 15°-30°E
8	South America (S. America)	18°-55°S, 65°-75°W
9	Australia	15°-35°S, 128-147°E

Table 2 Sensitivity of annual mean wind erosion threshold (m s^{-1}) to the selection of different retrieval criteria. Note the setting of the last column is the same as DOD_{thresh}=0.2 or 0.02, except surface DOD (sDOD) from Aqua is used over North Africa.

Regions	**Soil Moisture (cm^3 cm^{-3})**			**LAI (m^2m^{-2})**			**Snow coverage (%)**			**DOD_{thresh}**		
	<0.1	<0.15	None	<0.15	<0.3	<0.5	<=0.2	<=2	<=10	=0.2 (0.02)	=0.5 (0.05)	sDOD
Sahel	3.21	3.19	3.22	3.24	3.21	3.19	3.21	3.21	3.21	3.21	4.93	6.05
Sahara	4.61	4.56	4.49	4.54	4.61	4.59	4.61	4.61	4.61	4.61	7.59	7.66
AP	5.37	5.26	5.26	5.26	5.37	5.37	5.37	5.36	5.35	5.37	8.00	5.57
N. China	7.73	7.64	7.07	7.79	7.73	7.71	7.73	7.56	7.44	7.73	10.15	7.73
India	5.63	5.12	4.99	6.46	5.63	5.63	5.63	5.61	5.60	5.63	8.59	5.63
U.S.	5.71	5.23	4.98	6.53	5.71	5.56	5.71	5.60	5.41	5.71	7.04	5.71
S. Africa	5.41	5.23	5.20	6.72	5.41	5.10	5.41	5.40	5.40	5.41	6.46	5.41
S. America	6.46	6.32	6.20	6.88	6.46	6.39	6.46	6.39	6.35	6.46	8.20	6.46
Australia	5.19	5.16	5.14	5.66	5.19	5.22	5.19	5.19	5.19	5.19	6.49	5.19

Table 3 Sensitivity of annual mean wind erosion threshold (m s^{-1}) to surface wind speeds from different reanalyses (DOD_{thresh}= 0.2 or 0.02).

Regions	**Reanalysis**		
	NCEP	ERA-Interim	ERA5
Sahel	3.21	4.54	4.80
Sahara	4.61	5.56	5.63
AP	5.37	6.12	5.50
N. China	7.73	7.94	7.05
India	5.63	7.01	5.70
U.S.	5.71	6.82	6.18
S. Africa	5.41	7.17	6.26
S. America	6.46	7.51	6.36
Australia	5.19	7.36	6.68

Table 4 Simulation design

Simulations	**Wind erosion threshold**	**Source function**
Control	6 m s^{-1}	*S*
V_{thresh}12mn	12-month $V_{threshold}$	*S'*
V_{thresh}Ann	Annual mean $V_{threshold}$	*S'*

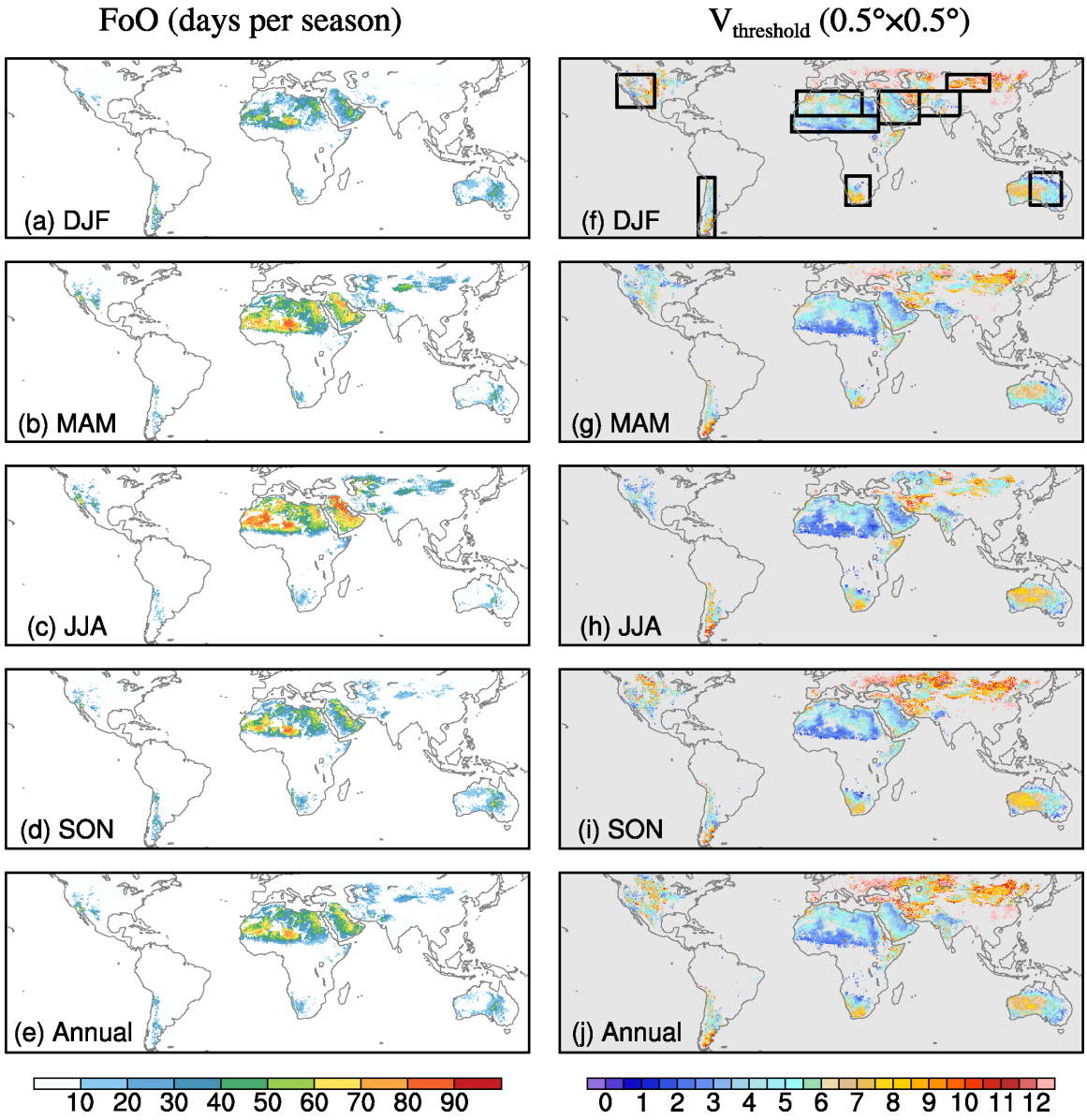

Figure 1. (a)-(e) Frequencies of occurrence (FoO; unit: days per season) in each season and annual mean. (f)-(j) Threshold of wind erosion ($V_{threshold}$; unit: m s^{-1}) derived from satellite products and reanalyses for each season and annual mean using DOD_{thresh} = 0.2 (or 0.02). Black boxes in (f) denote nine dust source regions as listed in Table 1.

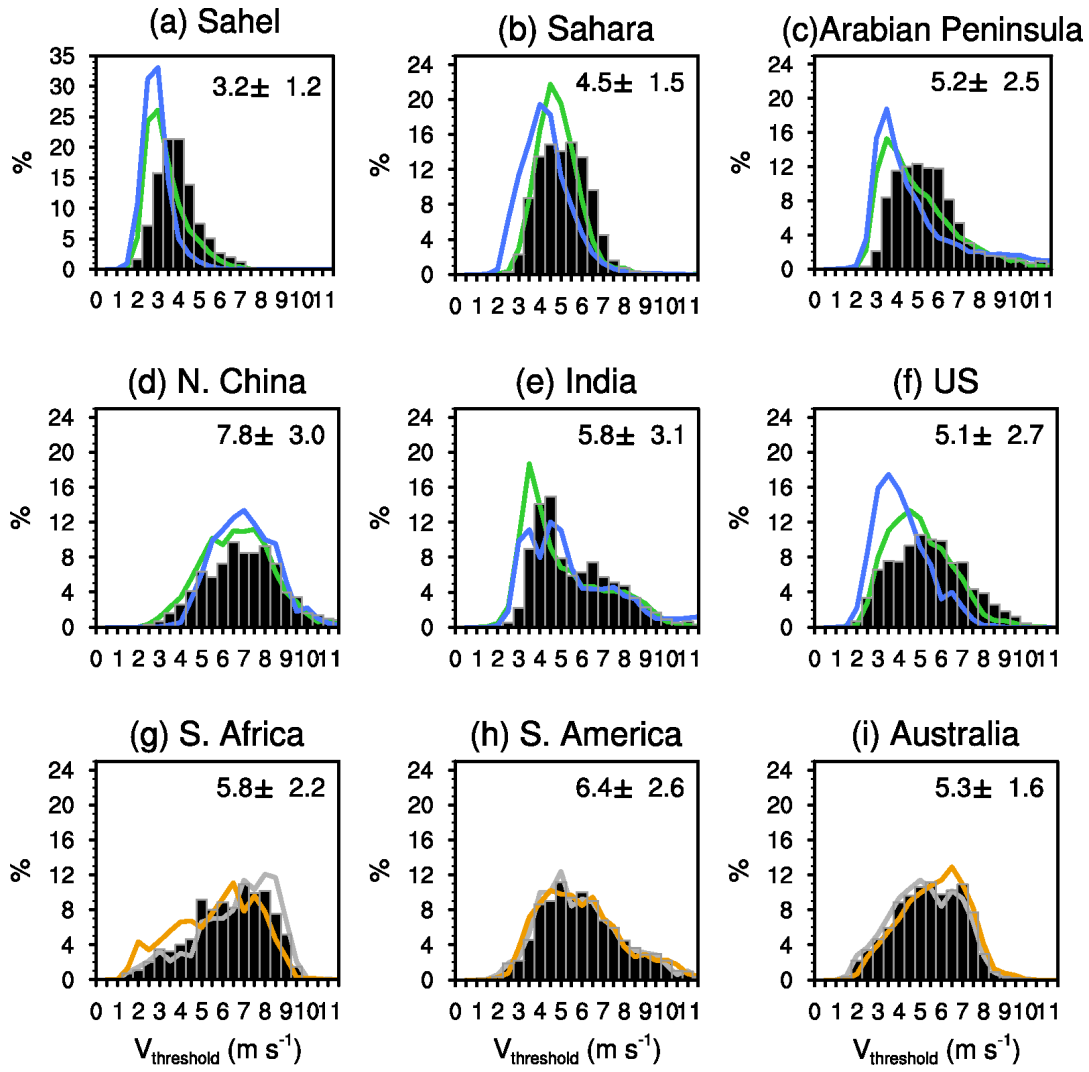

Figure 2. (a)-(i) Frequency distribution of annual mean $V_{threshold}$ (black bars) in each region (black boxes in Fig. 1) and for dusty seasons, i.e., MAM (green) and JJA (blue) for regions in the Northern Hemisphere and SON (orange) and DJF (grey) for regions in the Southern Hemisphere. The mean (averaged over all grid points in the region, without area weight) and ± one standard deviations of $V_{threshold}$ in each region are shown on the top right of each plot.

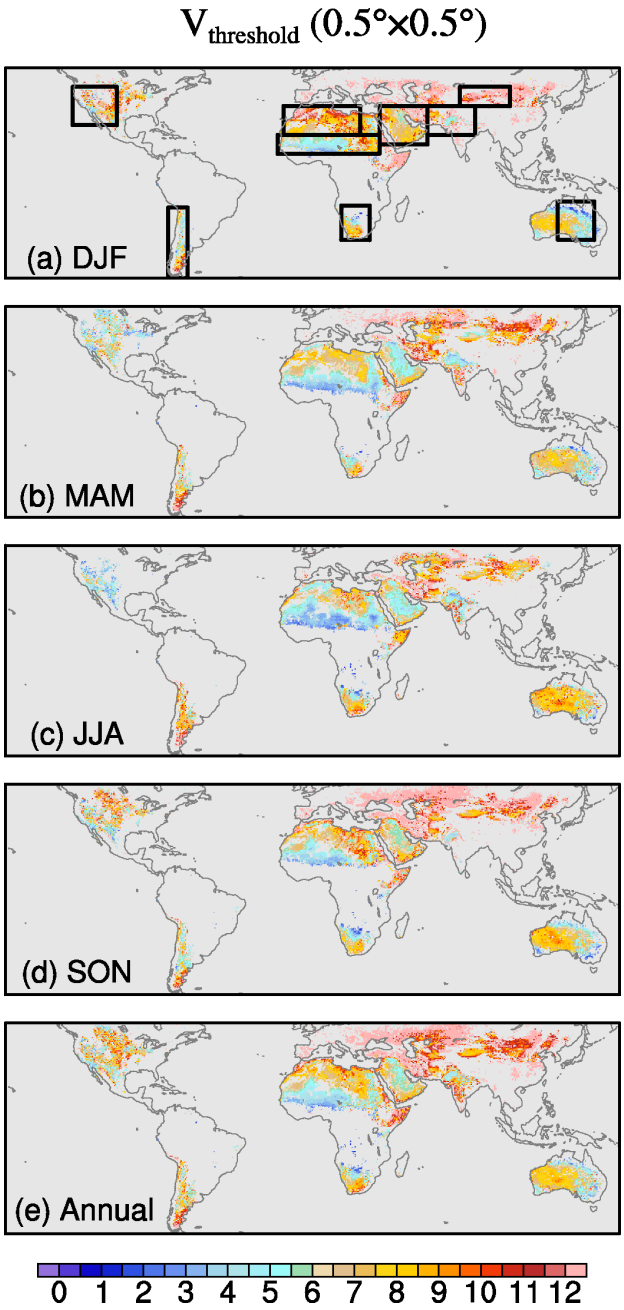

Figure 3. (a)-(e) Threshold of wind erosion ($V_{threshold}$; unit: m s^{-1}) derived from satellite products and reanalyses for each season and annual mean using DOD_{thresh}=0.5 (or 0.05). Black boxes in (a) denote nine dust source regions as listed in Table 1.

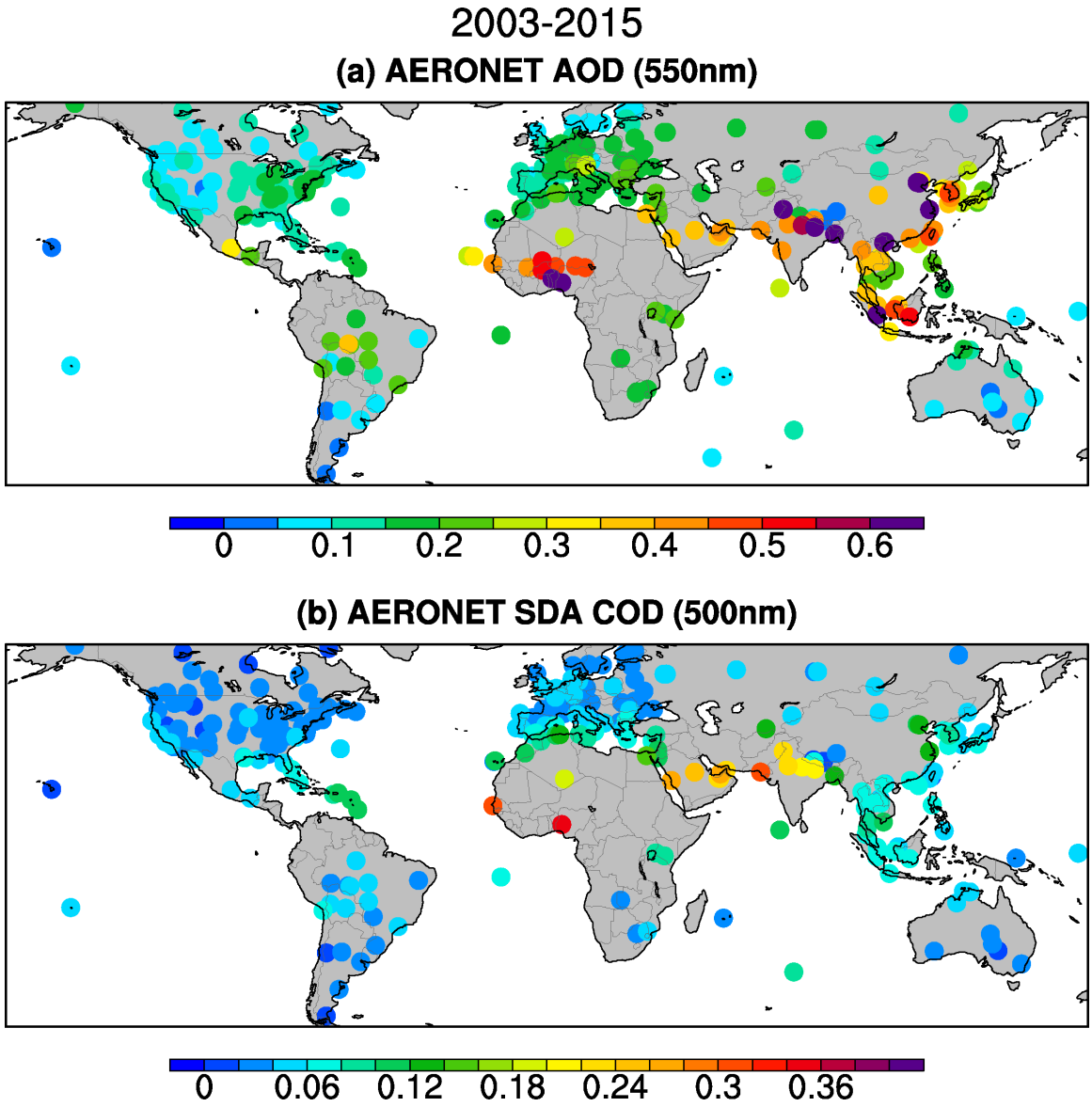

Figure 4. Climatology of annual mean AERONET (a) AOD (550 nm) and (b) SDA COD (500 nm) averaged over 2003-2015.

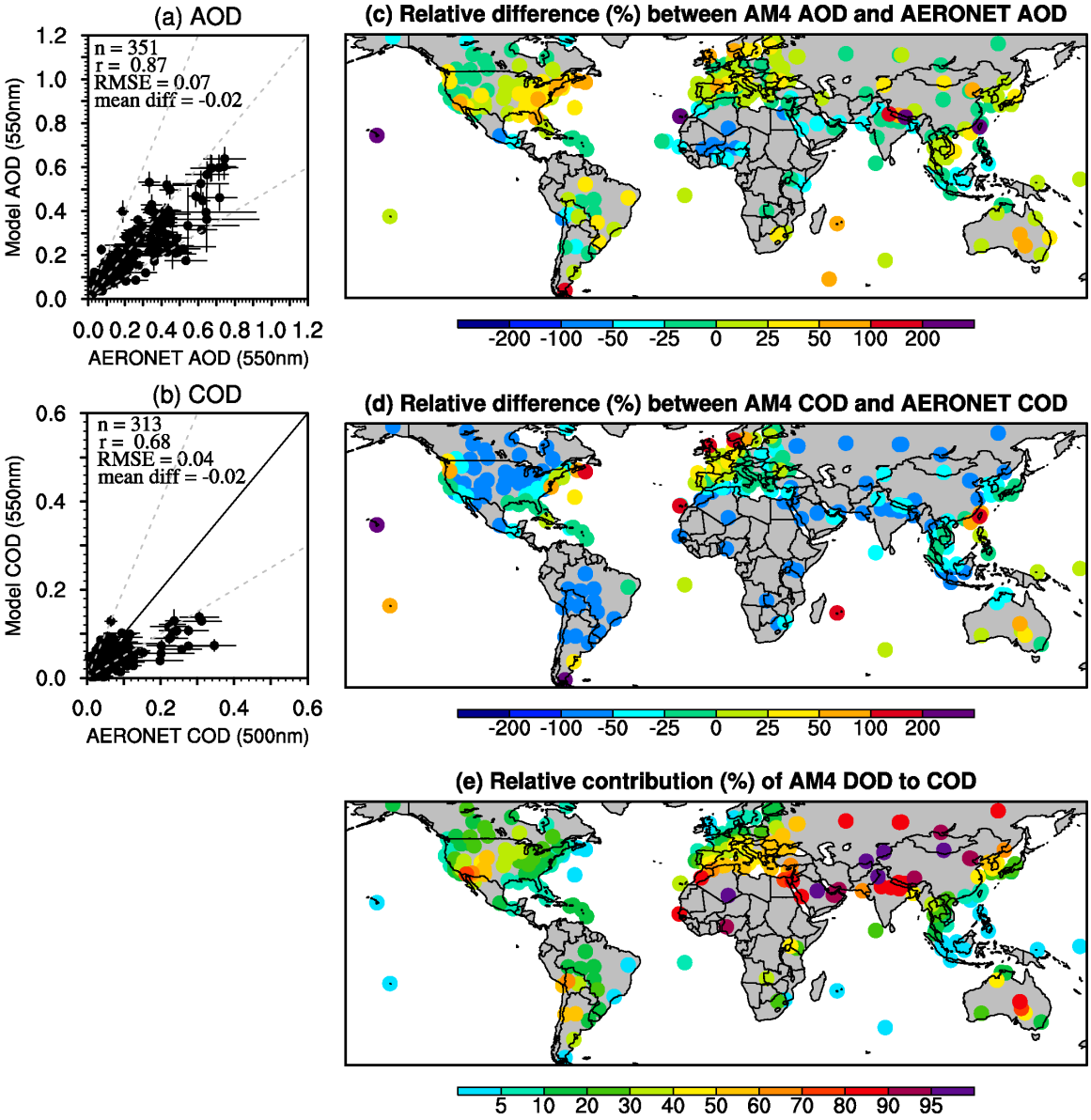

Figure 5. Scatter plot of simulated annual mean (a) AOD and (b) COD in the Control run versus AERONET AOD and COD (left), and the relative difference (in percentage) (c) between modeled AOD and AERONET AOD and (d) between modeled COD and AERONET COD (right). (e) The relative contribution of DOD to COD in the model.

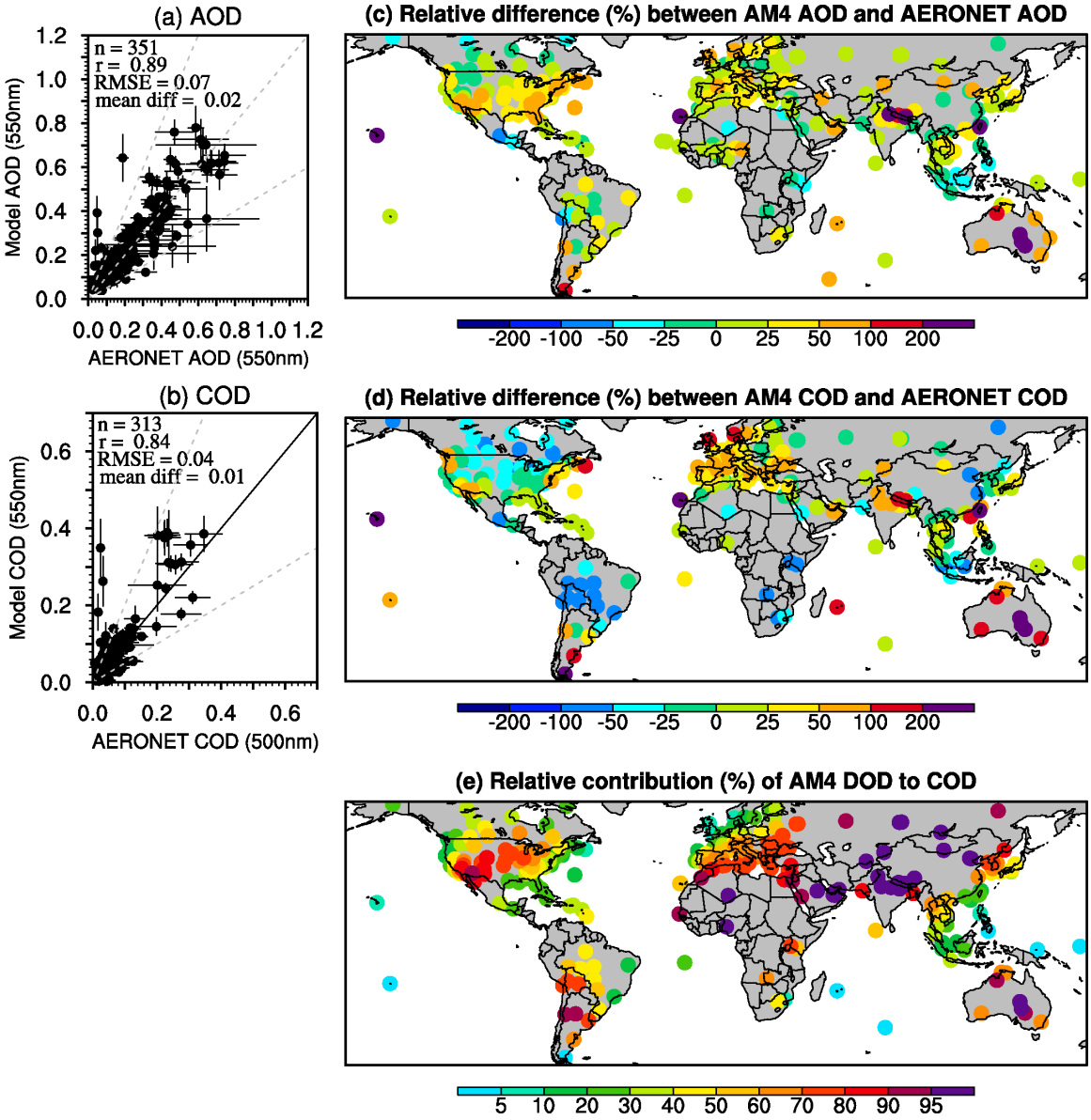

Figure 6. Same as Fig. 5 but for the V_{thresh}12mn simulation.

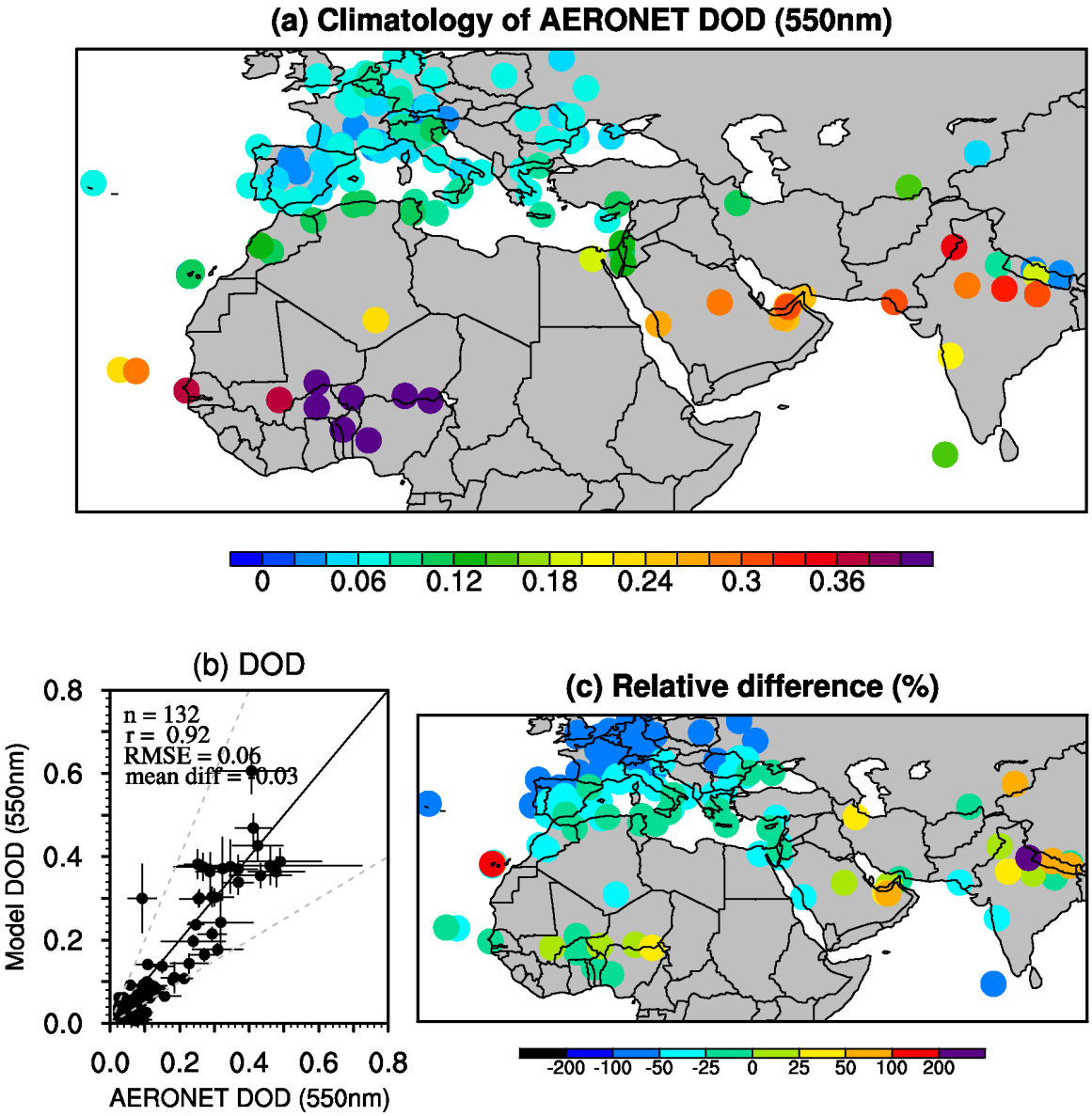

Figure 7. (a) Climatology (2003-2015) of AERONET DOD (550 nm) over major dusty regions and (b) scatter plot of modeled DOD in the V_{thresh}12mn simulation versus AERONET DOD, and (c) the relative difference (in percentage) between modeled DOD and AERONET DOD in the V_{thresh}12mn simulation.

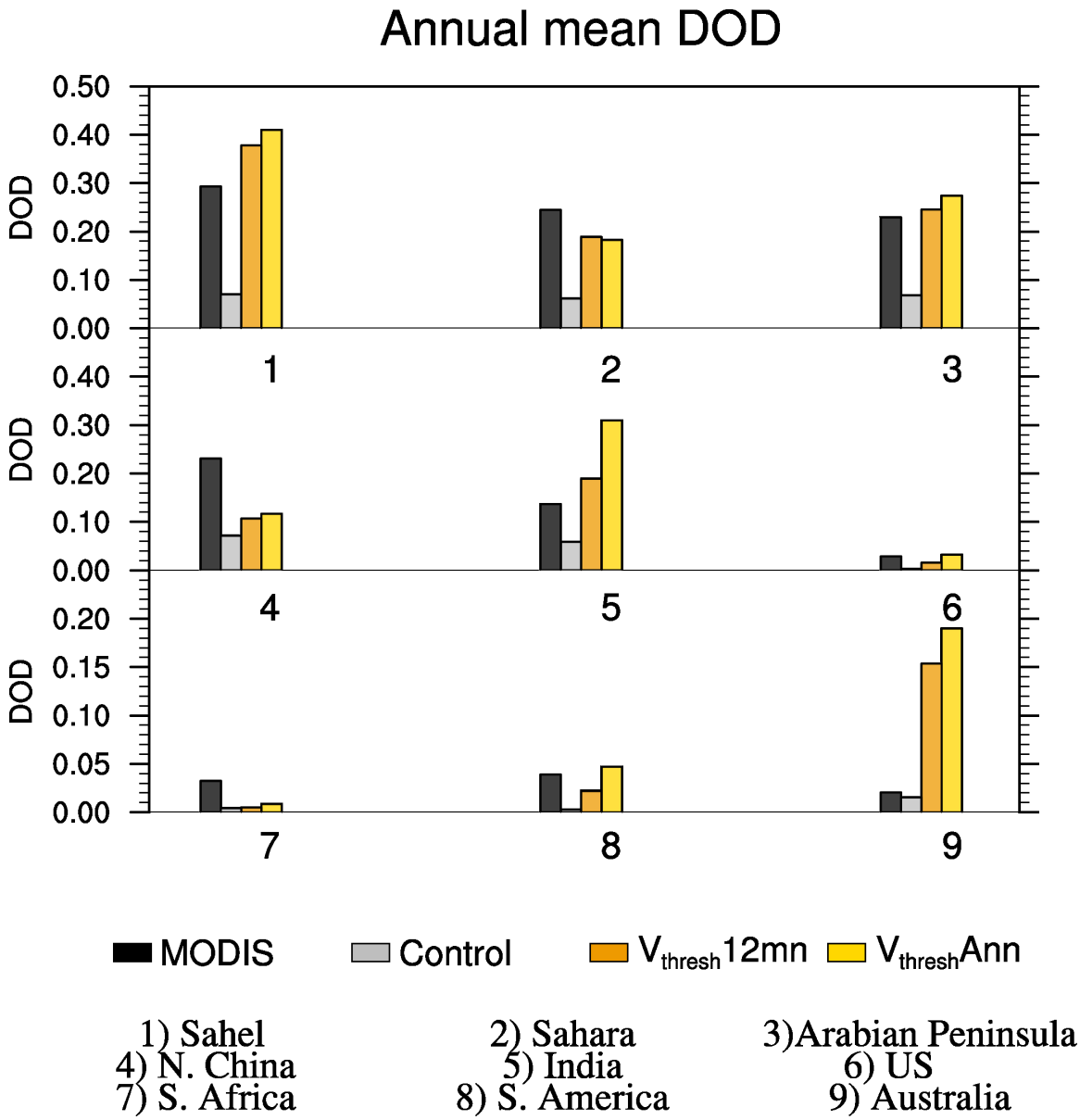

1643 Figure 8. Regional averaged annual mean DOD (2003-2015) over nine regions from the
1644 Control (grey), V_{thresh}12mn (orange), and V_{thresh}Ann (yellow) simulations and MODIS
1645 (black).
1646
1647
1648
1649
1650

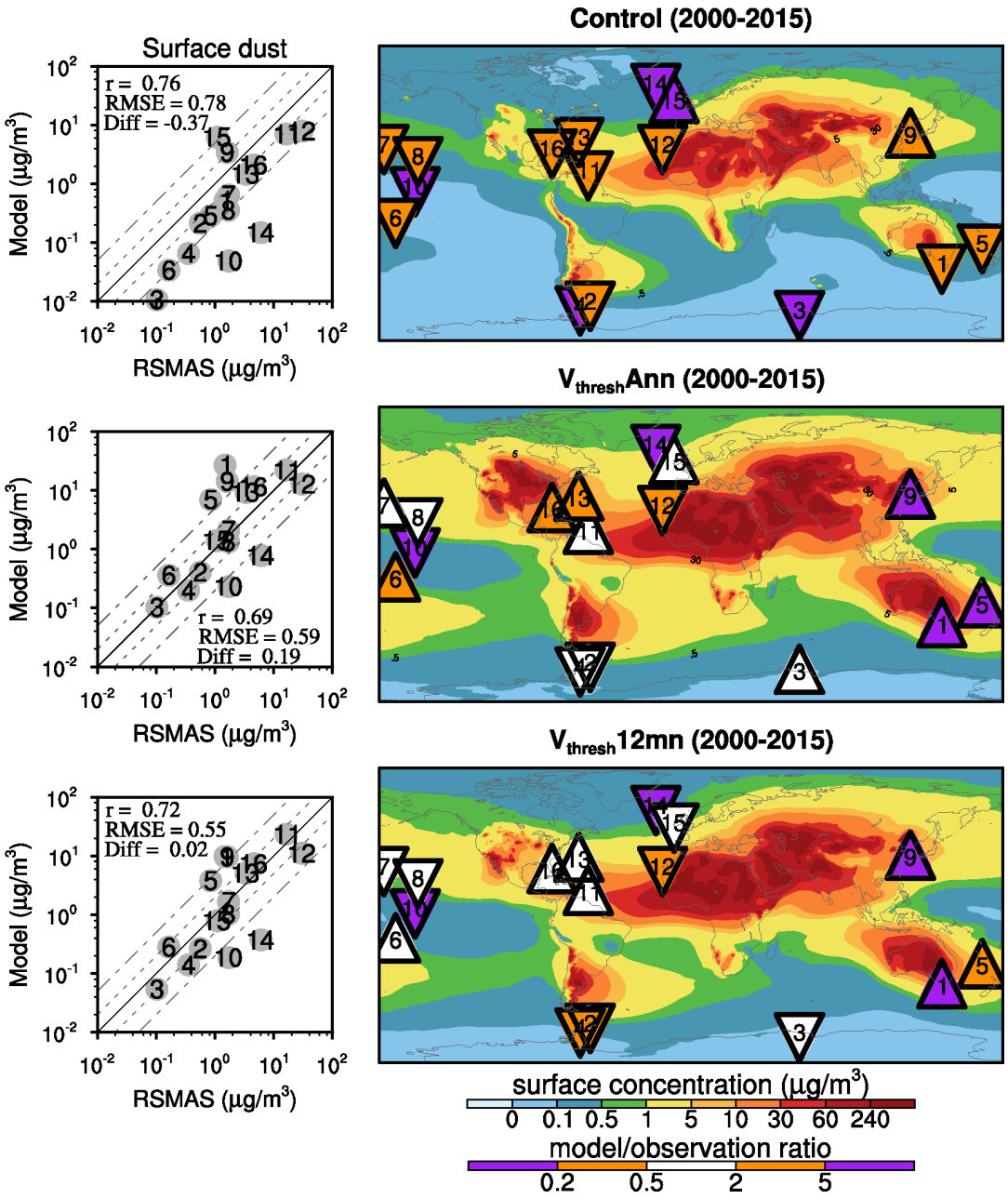

Figure 9. Scatter plots (left column) of model simulated (from top to bottom are the Control, V_{thresh}Ann, and V_{thresh}12mn simulations) surface dust concentration (µg m^{-3}) versus the climatology of observed surface dust concentration from RSMAS stations (Savoie and Prospero 1989), and spatial pattern of surface dust concentration from model output (shading; right column) and the ratio between modeled and RSMAS station observed surface dust concentration (color triangles, with upward triangles indicating overestimation and downward triangles indicating underestimation). 16 stations were used, and numbers in each triangle (right) and grey dots (left) indicate the stations. The one-one, one-two and one-five lines are plotted in solid, dashed and dash-dotted lines in the scatter plots. Statistics in the scatter plots are calculated in logarithmic space.

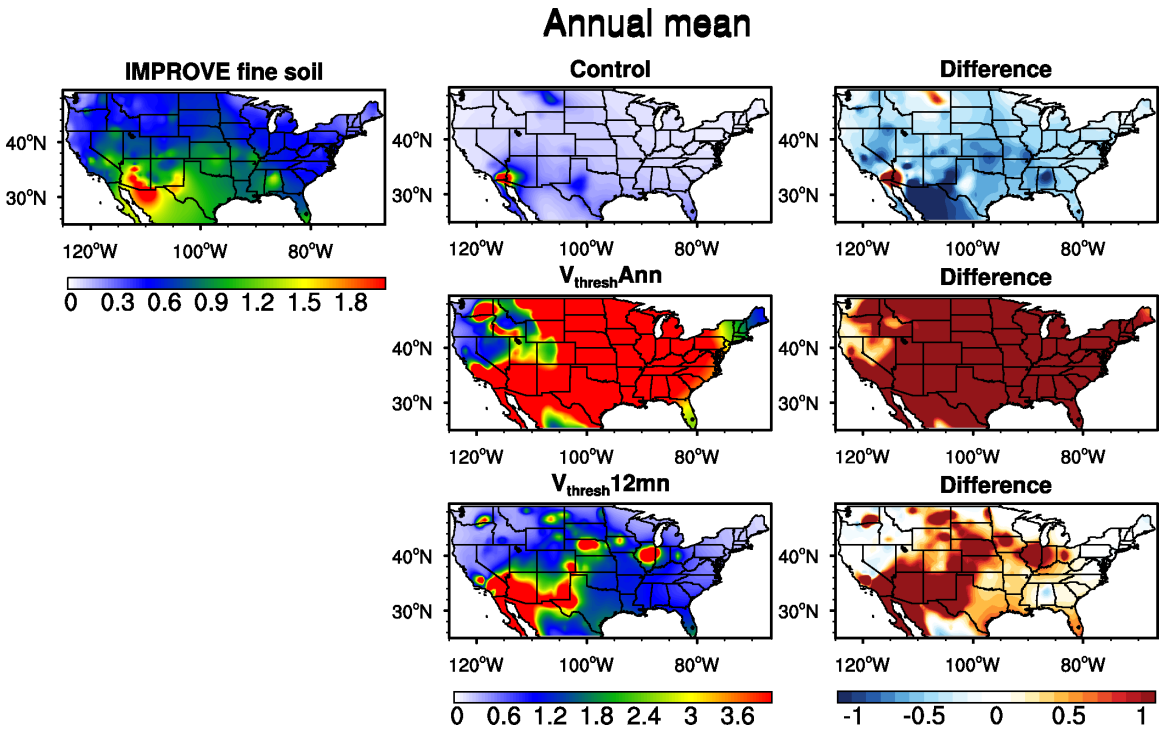

Figure 10. Annual mean surface fine dust concentration (μg m^{-3}) from IMPROVE stations (left column) and three simulations (middle column) and the differences between model and observation (right column) for 2002-2015.

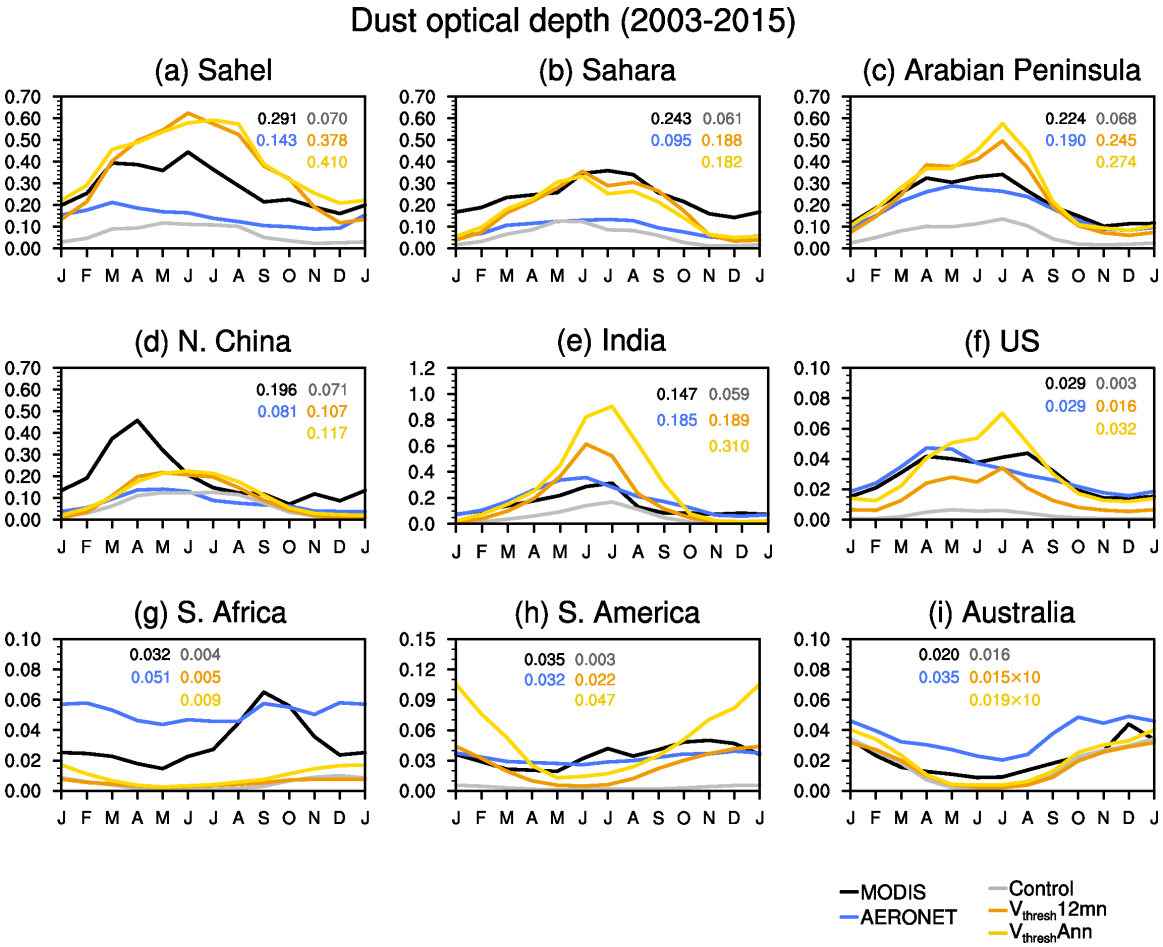

Figure 11. Seasonal cycle of DOD from MODIS (black), the Control (grey), V_{thresh}12mn (orange), and V_{thresh}Ann (yellow) runs, and gridded AERONET SDA COD (blue) averaged over nine regions. The annual mean of each dataset in each region is listed on the top of the plot.

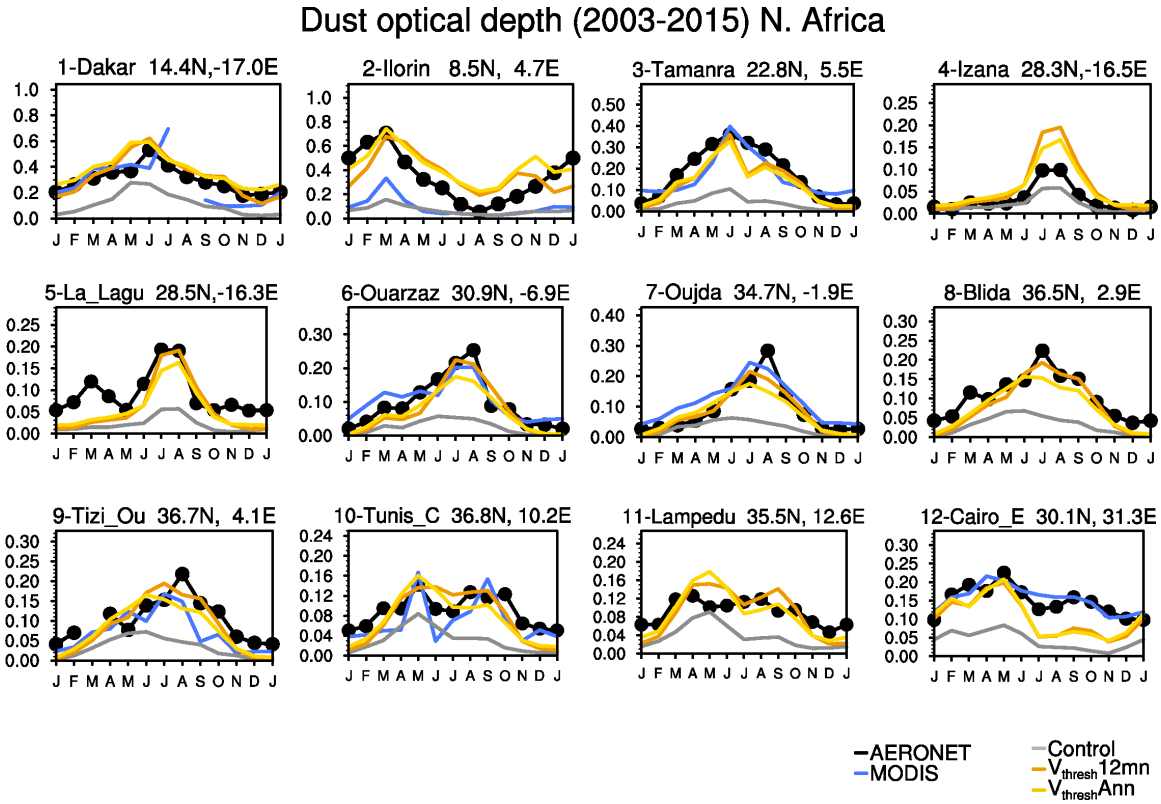

Figure 12. Seasonal cycle of DOD over 12 AERONET SDA sites (see Fig. S7 in the Supplement for locations) from the Control (grey), V_{thresh}12mn (orange), and V_{thresh}Ann (yellow) simulations, along with DOD from MODIS (blue), and COD from AERONET (black dotted line). All values are averaged over 2003-2015. The location (lat/long) and the name (due to space, only first seven characters are shown) of the sites are listed at the top of each plot.

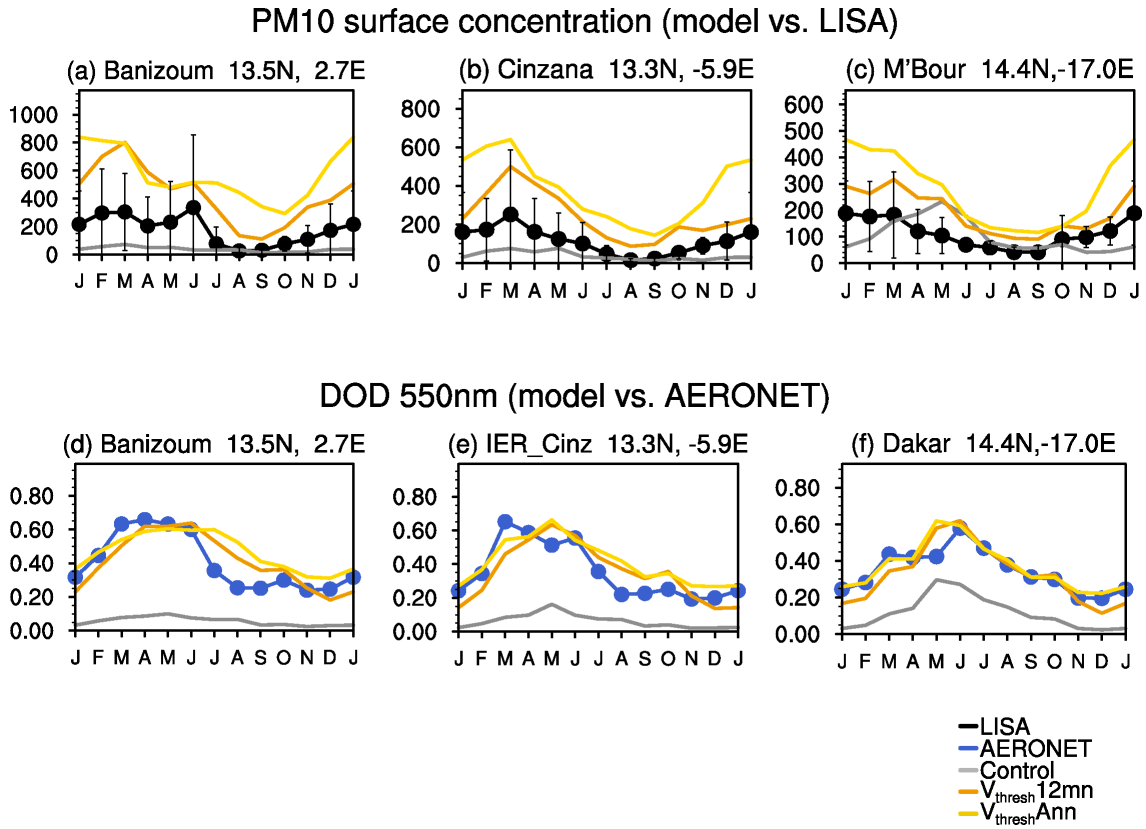

Figure 13. (a)-(c) Seasonal cycle of PM_{10} surface concentration (black) over three sites from the LISA project, along with PM_{10} surface dust concentration from the Control (grey), $V_{thresh}12mn$ (orange), and $V_{thresh}Ann$ (yellow) simulations. Error bars are ± one standard deviations of daily mean in each month averaged over 2006-2014. Unites: μg m^{-3}. (d)-(f) seasonal cycle of DOD (550 nm) from three AERONET sites co-located with LISA sites (blue) versus that modeled by the Control (grey), $V_{thresh}12mn$ (orange), and $V_{thresh}Ann$ (yellow) simulations.

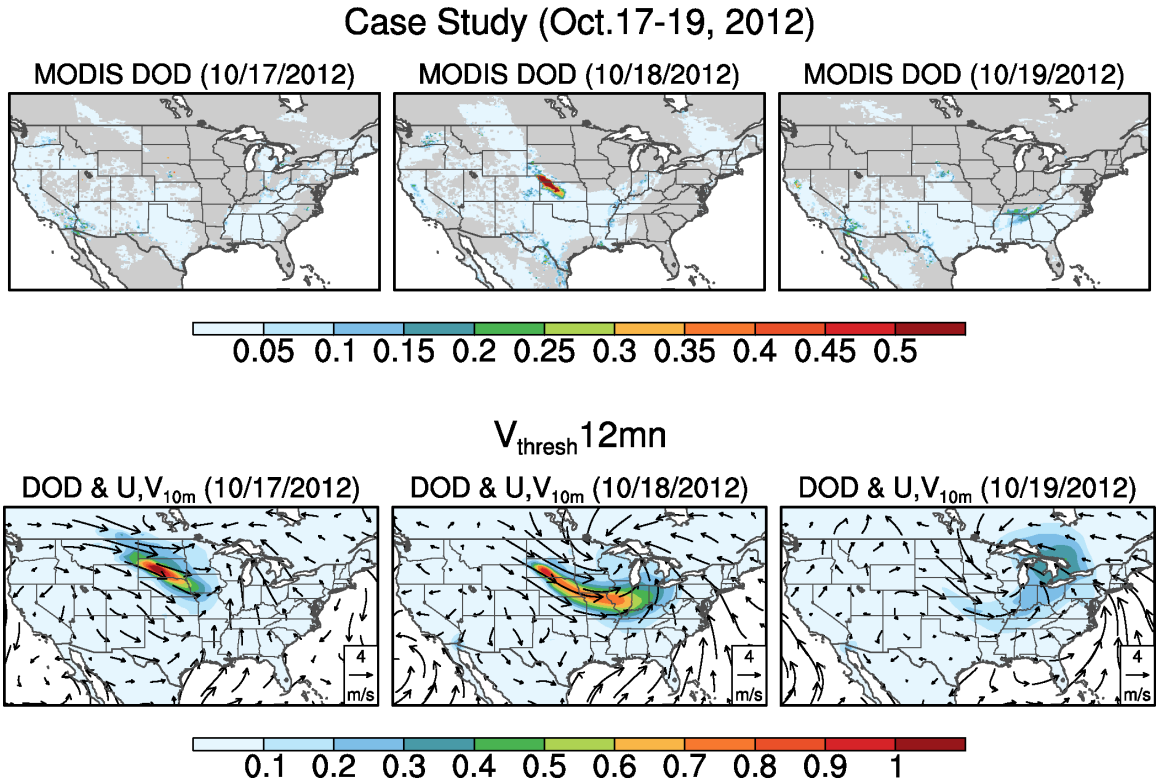

Figure 14. Daily DOD from MODIS (top panel), daily DOD simulated by the V_{thresh}12mn run along with anomalies (with reference to the 2000-2015 mean) of surface wind vectors (m s^{-1}; bottom panel) from Oct. 17th to Oct. 19th, 2012. Only DOD over land is shown. Missing values in MODIS DOD (top panel) are plotted in grey shading.

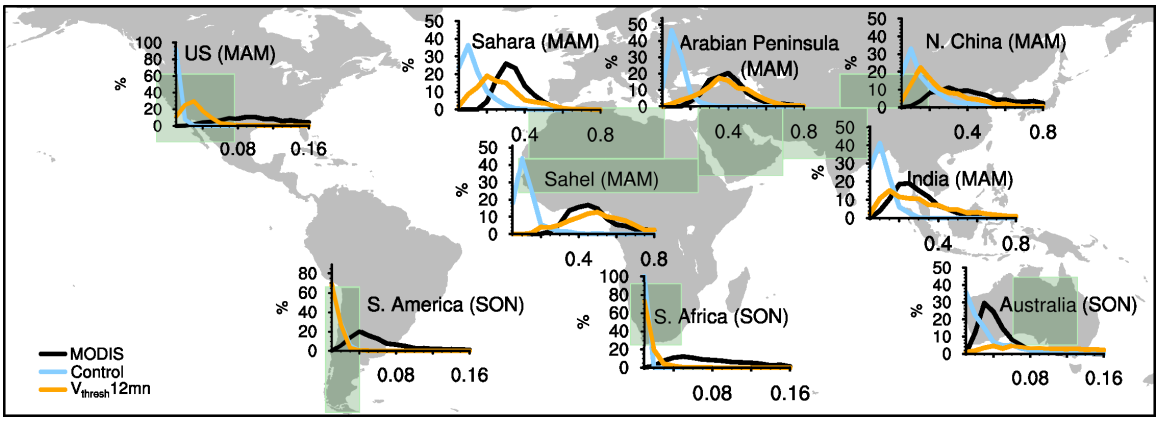

Figure 15. Frequency (%) distribution of regional averaged daily DOD from MODIS (black) versus that from the Control (light blue) and V_{thresh}12mn (orange) simulations for the Sahara, the Sahel, the Arabian Peninsula, northern China, India, western to central U.S., South America, South Africa, and Australia from 2003 to 2015. X-axis denotes the ranges of DOD (the bin spacing for dusty regions is 0.05 and for less dusty regions is 0.01), and y-axis is percentage of occurrence. The light green boxes denote the averaging areas. For regions in the Northern Hemisphere frequency in MAM is shown, while for regions in the Southern Hemisphere frequency in SON is shown.